nature communications

Article

https://doi.org/10.1038/s41467-024-53264-8

TGF-β-mediated crosstalk between TIGIT$^+$ Tregs and CD226$^+$CD8$^+$ T cells in the progression and remission of type 1 diabetes

Received: 19 October 2023

Accepted: 8 October 2024

Published online: 15 October 2024

Check for updates

Ting Zhong[1,6], Xinyu Li[1,6], Kang Lei[1,6], Rong Tang[1], Qiaolin Deng[2], Paul E Love[3], Zhiguang Zhou[1] ✉, Bin Zhao[1,4,5] ✉ & Xia Li[1] ✉

Type 1 diabetes (T1D) is a chronic autoimmune condition characterized by hyperglycemia resulting from the destruction of insulin-producing β-cells that is traditionally deemed irreversible, but partial remission (PR) with temporary reversal of hyperglycemia is sometimes observed. Here we use single-cell RNA sequencing to delineate the immune cell landscape across patients in different T1D stages. Together with cohort validation and functional assays, we observe dynamic changes in TIGIT$^+$CCR7$^-$ Tregs and CD226$^+$CCR7$^-$CD8$^+$ cytotoxic T cells during the peri-remission phase. Machine learning algorithms further identify TIGIT$^+$CCR7$^-$ Tregs and CD226$^+$CD8$^+$ T cells as biomarkers for β-cell function decline in a predictive model, while cell communication analysis and in vitro assays suggest that TIGIT$^+$CCR7$^-$ Tregs may inhibit CD226$^+$CCR7$^-$CD8$^+$ T cells via TGF-β signaling. Lastly, in both cyclophosphamide-induced and streptozotocin (STZ)-induced mouse diabetes models, CD226 inhibition postpones insulitis onset and reduces hyperglycemia severity. Our results thus identify two interrelated immune cell subsets that may serve as biomarkers for monitoring disease progression and targets for therapeutic intervention of T1D.

Type 1 diabetes (T1D) is a progressive autoimmune disease that currently affects approximately 8.4 million people worldwide, with prevalence increasing by approximately 4% per year[1,2]. Accumulating evidence has linked T1D etiology to a combination of genetic and environmental factors which eventually results in the breakdown of immunological tolerance, thus treatment strategies focusing on immunomodulation are considered to be the most promising. The recent approval by the USA Food and Drug Administration (FDA) of the first disease-modifying therapy for T1D, the anti-CD3 monoclonal antibody Teplizumab, ushers in a new era in the treatment of T1D[3–5]. Despite these extensive efforts, detailed immunopathological mechanisms during the different stages of T1D remain elusive[6,7].

T1D involves complex interactions between islet β cells and the immune systems[8,9]. Especially, an imbalance between CD8$^+$ T cells and regulatory T cells (Tregs) has been highlighteted, and diabetogenic CD8$^+$ T cell precursors are present in the pancreas-draining lymph node (PLN), where they may continuously generate effector cells and migrate to the pancreas, destroying β cells and eventually causing T1D[9–13]. However, most of these studies came from mouse models, limiting their application in clinical settings. Also, detecting T1D-specific immune cell subsets from peripheral blood would be ideal due

[1]National Clinical Research Center for Metabolic Diseases, Key Laboratory of Diabetes Immunology, Ministry of Education, and Department of Metabolism and Endocrinology, The Second Xiangya Hospital of Central South University, Changsha, Hunan, China. [2]Department of Physiology and Pharmacology, Karolinska Institute, 17177 Solna, Sweden. [3]Section on Hematopoiesis and Lymphocyte Biology, Eunice Kennedy Shriver National Institute of Child Health and Human Development, National Institutes of Health, Bethesda, MD, USA. [4]CSU-Sinocare Research Center for Nutrition and Metabolic Health, Xiangya School of Public Health, Central South University, Changsha, Hunan, China. [5]Furong Laboratory, Changsha, Hunan, China. [6]These authors contributed equally: Ting Zhong, Xinyu Li, Kang Lei. ✉e-mail: zhouzhiguang@csu.edu.cn; binzhao@csu.edu.cn; lixia@csu.edu.cn

to the easy availability. Therefore, a comprehensive assessment of the peripheral immune cells involved in different stages of T1D is warranted.

Shortly after T1D diagnosis and initiation of insulin therapy, some patients may undergo a phase of partial remission (PR). Previous research conducted by our team and others has revealed that the immune profiles and intracellular metabolism of T cells during this specific period display distinct features from newly onset ones[14–18], providing a natural model for investigating the restoration of immune tolerance toward β cells within the context of T1D. However, the characteristics of immune cells in PR phase, particularly T cells subsets, remain unclear.

Immune checkpoint receptors play an essential role in maintaining the equilibrium of T-cell immunity by regulating the balance between co-stimulatory and inhibitory signals[19,20], which are also implicated in the pathogenesis of T1D[21,22]. Recently, an intriguing immune checkpoint system has come to light, featuring CD226 as the co-stimulatory receptor and T cell immunoglobulin and ITIM domain (TIGIT) as the co-inhibitory receptor. TIGIT and CD226 compete for the binding of ligands CD112/CD155, and the delicate balance between the co-stimulatory effects of CD226 and the co-suppressive functions of TIGIT plays a crucial role in the maintenance of immune homeostasis[23–25]. In this regard, Thirawatananond, P et al. demonstrated that nonobese diabetic (NOD) mice lacking CD226 were protected from the onset of T1D[26]. However, the precise impact of CD226/TIGIT on T-cell function during the progression and remission of T1D, particularly their alterations and regulatory mechanisms, remains poorly understood.

In this study, we identify TIGIT$^+$CCR7$^-$ Tregs and CD226$^+$CD8$^+$ T cells as crucial biomarkers during the peri-remission phase of T1D. TIGIT$^+$CCR7$^-$ Tregs promote immune tolerance in PR phase by inhibiting CD226$^+$CD8$^+$ T cell activation via TGF-β1 signaling. Blocking CD226 delays insulitis and the onset of diabetes, and reduces hyperglycemia in both cyclophosphamide (Cy) and streptozotocin (STZ)-induced mouse diabetes models. Our findings spotlight two interrelated immune cell subsets with roles in T1D progression and PR, and present promising targets for future T1D immunotherapies.

Results

A single-cell peripheral immune atlas of T1D

To understand the heterogeneity of immune cells across the different stages of T1D, single-cell RNA sequencing (scRNA-seq) was performed to interrogate the transcriptomic status of peripheral immune cells. In total, 12 patients were enrolled, including 5 new-onset cases with T1D (New), 4 cases during PR with T1D, and 3 HDs. A schematic illustration summarizing the clinical information for the individuals involved is shown in Fig. 1A[27]. An overview of the approach and clustering strategy used to analyze the circulating immune cell profiles is summarized in Fig. 1B.

After quality control and batch correction (supplementary Fig. 1), 139,901 cells were retained for analysis, including 44,508 cells from T1D patients and 95,393 cells from HDs (supplementary Table. 1). Thirteen cell types were manually identified based on CellTypist annotation results (supplementary Fig. 2) and the expression of canonical marker genes (supplementary Table 2, supplementary Dataset 1). Most of the peripheral immune cell types could be captured

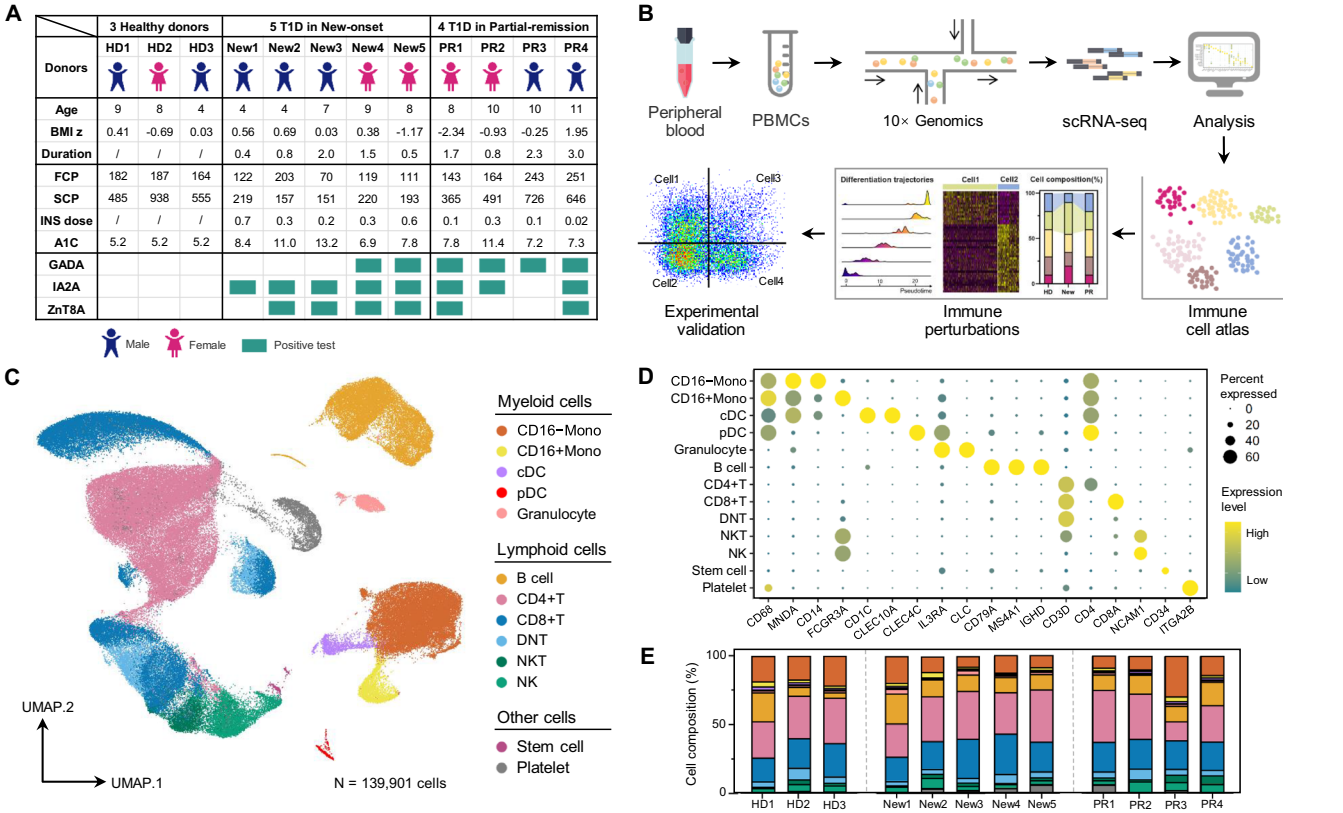

Fig. 1 | Overview of the peripheral immune landscape in patients in different T1D phases and HD. A Schematic illustration highlighting the group design and clinical information for the individuals. **B** Schematic diagram highlighting the workflow of the study design and analysis. **C** UMAP embedding overlaid with unsupervised cluster cell type annotations. **D** Dot plot showing the expression levels of canonical markers in each cell type. The dot size indicates the expression of the gene cluster as a percentage. **E** Major cell-type compositions for each individual. The cell types represented by the color correspond to Fig. 1C. T1D, type 1 diabetes; NEW, new-onset; PR, partial remission; HD, healthy donor; PBMCs, peripheral blood mononuclear cells; scRNA-seq, single-cell RNA sequencing. Source data are provided as a Source Data File.

https://doi.org/10.1038/s41467-024-53264-8

by the scRNA-seq, including CD16$^+$ monocytes (CD16$^+$ Mono), CD16$^-$ monocytes (CD16$^-$ Mono), conventional dendritic cells (cDCs), plasmacytoid dendritic cells (pDCs), granulocytes, B cells, CD4$^+$ T cells (CD4$^+$ T), CD8$^+$ T cells (CD8$^+$ T), double negative T cells (DNT), natural killer cells (NK), natural killer T cells (NKT), and a small number of stem cells and platelets (Fig. 1C, D). The small number of granulocytes and platelets may be related to technical factors introduced during sample collection and processing. Quality control analysis revealed that granulocytes and platelets exhibited lower total counts and gene features (supplementary Fig. 1) and were therefore considered low-quality cells. A global view of the cell composition data from each donor was generated to illustrate the cell composition differences. The composition variability within groups was detected and showed individual heterogeneity (Fig. 1E). In summary, the first peripheral immune landscape was mapped for T1D progression and PR at a single-cell resolution.

ScRNA-seq revealed a role of TIGIT$^+$ CCR7$^-$ Tregs in different stages of T1D

A total of 6 typical CD4$^+$ T cell clusters were identified, including naive (Tn), central memory (Tcm), T helper type 1 (Th1), T helper type 2 (Th2), T helper type 17 (Th17) and Tregs (Fig. 2A). Each CD4$^+$ T cell cluster exhibited distinct signature genes and transcription factors (TFs) (Fig. 2B, C). The composition variability of CD4$^+$ T subclusters within groups was insignificant although individual heterogeneity was detected (Fig. 2D, supplementary Fig. 3A). However, differential gene analysis suggested that the transcriptional profile of CD4$^+$ T cells was not entirely the same at different stages of T1D (supplementary Fig. 3B). Interestingly, regulon activity analysis revealed that transcription factor *STAT5B* was more activated in the Tn and Tcm cells in new-onset cases. In contrast, *HMGB2*, *JUND*, *KLF2*, *CEBPB*, *IRF9* and *YBX1* were downregulated in the new-onset group and recovered in the PR phase (supplementary Fig. 3C). While the regulon models in Th1 cells showed dynamic changes in two transcription factors *NFATC2* and *KLF2* at different stages of T1D (supplementary Fig. 3D).

CD4$^+$ Tregs were identified by markers for interleukin 2 receptor subunit alpha (IL2RA, also known as CD25), forkhead box P3 (FOXP3) and cytotoxic T-lymphocyte associated protein 4 (CTLA4). By re-clustering, the heterogeneity of the Tregs was assessed and seven clusters were generated (c1–c7) with clearly defined marker genes (Fig. 2E, supplementary Fig. 4A). Based on the expression levels of TIGIT and CCR7, three Treg phenotypes (TIGIT$^-$CCR7$^+$ Tregs, TIGIT$^+$CCR7$^+$ Tregs, TIGIT$^+$CCR7$^-$ Tregs) were annotated (Fig. 2F, G). The compositions of the Treg subsets were altered in different disease stages. Specifically, when compared to the HD group, the frequencies of TIGIT$^+$CCR7$^-$ Tregs decreased in new-onset patients, increased to a

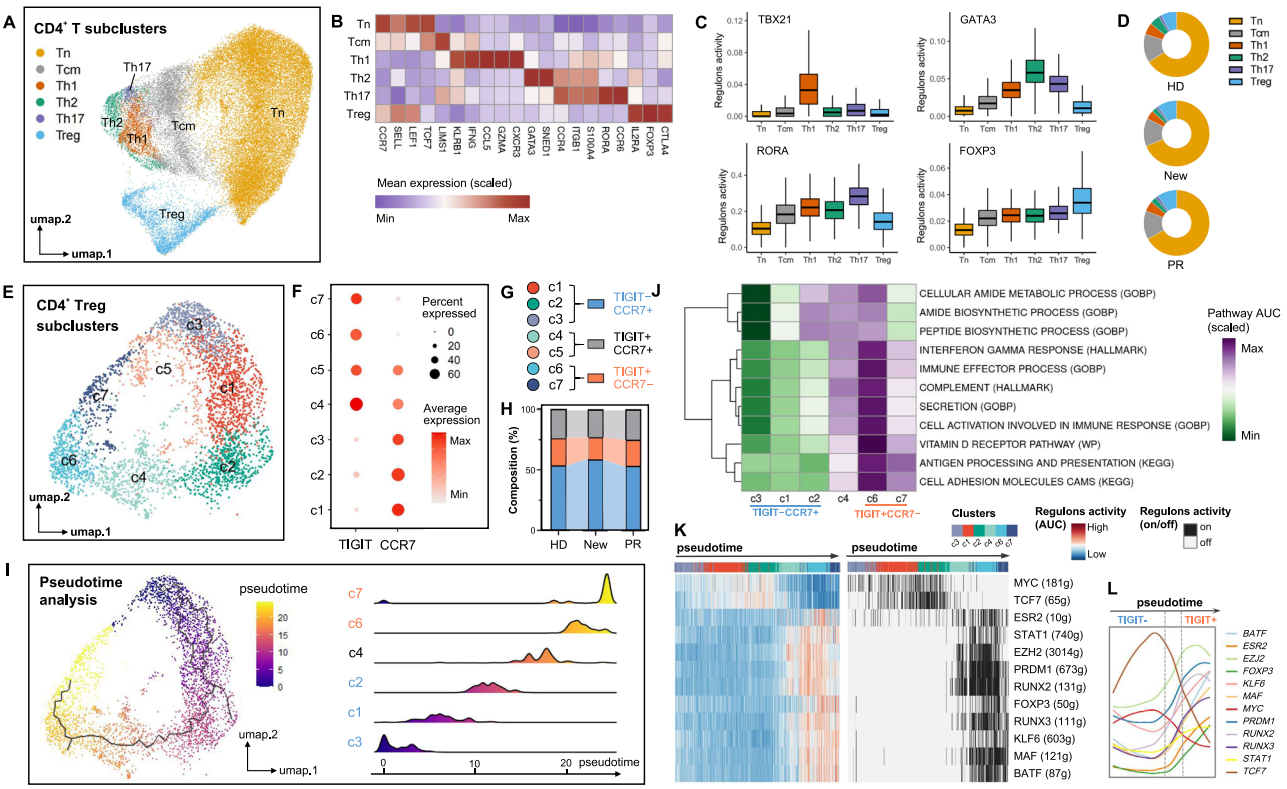

Fig. 2 | Dynamic changes in the composition and differentiation trajectories of the Treg subclusters in different T1D phases. A UMAP visualization of the CD4$^+$ T cell subclusters. **B** Heatmap showing the scaled expression levels of canonical markers in each cell type. **C** Regulon activity of transcription factors within each type of CD4$^+$ T cell. Data from 40,040 CD4$^+$ T cells are shown: Tn (n = 27,004), Tcm (n = 5,584), Th1 (n = 1,903), Th2 (n = 1,371), Th17 (n = 535), and Treg (n = 3,640). Each cell represents a biological replicate. The central line in the box denotes the median of activity values. The box represents the interquartile range (IQR), bounded by the 25th percentile (lower quartile) and the 75th percentile (upper quartile). Whiskers extend from the box to the largest and smallest values within 1.5 × IQR from the quartiles. Data points outside this range are considered outliers and are not displayed. **D** Composition of CD4$^+$ T cells in each group. **E** UMAP visualization of the CD4$^+$ Treg subclusters. **F** Dot plot showing the expression levels of the TIGIT and CCR7 in each Treg subcluster. **G** Annotation of the Treg phenotypes based on the expression levels of the TIGIT and CCR7. **H** Treg phenotype compositions of each group. **I** UMAP visualization showed a differentiation trajectory for Treg predicted by Monocle 3. Cells were ordered in pseudotime by a gradient coloring from purple to yellow. Density distribution plots displayed the compositions of the Treg subclusters over pseudotime. **J** Scaled AUC values of the differential signaling pathways in each Treg subcluster and (**K**) activity of TF regulons that were differential between the TIGIT$^-$CCR7$^+$ and TIGIT$^+$CCR7$^-$ Tregs. Regulon activity was shown as the AUC value (left) and dichotomous activation status (right). Cells were sorted by pseudotime and subclusters. **L** Alterations in regulon activity under pseudotime differentiation trajectories. T1D, type 1 diabetes; NEW, new-onset; PR, partial remission; HD, healthy donor. Source data are provided as a Source Data File.

normal level during the PR period, and significantly declined in post-PR patients. In contrast, we noted an increasing trend in the proportion of CCR7$^+$TIGIT$^-$ Tregs in the new-onset group, alongside a decreasing trend during the PR period (Fig. 2H).

To further explore the continuum of development states in the Treg clusters, pseudotime analysis using Monocle 3 was conducted. Starting from c3, we reconstructed a potential differentiation trajectory in Tregs (Fig. 2I). The trajectory proceeded from TIGIT$^-$CCR7$^+$ Tregs (c3, c1, c2) to TIGIT$^+$CCR7$^+$ Tregs (c4), and then to TIGIT$^+$CCR7$^-$ Tregs (c6, c7), which meant that the TIGIT increased and CCR7 decreased along with the process (Fig. 2I). Functional genes were identified for the Tregs such as *IL2RA*, *TGFB1*, and *CTLA4* and they were synchronously increased with pseudotime (supplementary Fig. 4B). The c5 cluster may be in an abnormal cell state due to obvious outliers in the pseudotime analysis. Furthermore, considering the extremely small size of the c5 cluster, it was not included in the analysis.

To compare the signal transduction signatures of different Treg subsets, pathway activity analysis was performed using AUCell. The activity analysis identified variations in multiple signaling pathways. The pathways related to type I interferon (IFN) gamma response, immune effector process, cytokine secretion, and cell adhesion were stronger in TIGIT$^+$CCR7$^-$ Tregs (c6, c7) than in TIGIT$^-$CCR7$^+$ Tregs (c1, c2, c3) (Fig. 2J, supplementary Fig. 5). To understand the transcriptional regulatory features of different Treg clusters and construct a regulatory network, we further mapped the TF regulon landscape using single-cell regulatory network inference and clustering (SCENIC) analysis and identified 12 TFs with obvious differences. These TFs with regulons exhibited distinct activation signatures across subclusters under pseudotime differentiation trajectories. MYC and TCF7 were mainly activated in the TIGIT$^-$CCR7$^+$ Treg subclusters (c1, c2, c3), while *ESR2*, *STAT1*, *EZH2*, *PRDM1*, *RUNX2*, *FOXP3*, *RUNX3*, *KLF6*, *MAF*, and *BATF* were mainly activated in TIGIT$^+$CCR7$^-$ Tregs (c4, c6, c7) (Fig. 2K, supplementary Fig. 6). Combined with the pseudotime trajectory, TIGIT and CCR7 expression was closely related to the regulons' activity (Fig. 2L).

ScRNA-seq revealed a role of CD226$^+$CCR7$^-$CD8$^+$ T cells during different phases of T1D

CD8$^+$ T cell heterogeneity was assessed and 18 CD8$^+$ T cell subclusters were defined (c1–c18) (Fig. 3A). Based on the expression levels of CCR7 and KLRG1, KLRG1$^-$CCR7$^+$ naive (Tn) and central memory (Tcm) cells were annotated, and the remaining effector or memory CD8$^+$ T cells (c4, c7, c8, c10, and c15) were screened for further analysis (Fig. 3B). The CCR7$^-$CD8$^+$ T cell subsets were then re-annotated based on the expression levels of the CD226 and TIGIT (Fig. 3C–F). These CCR7$^-$CD8$^+$ T cells could be divided into 3 separate phenotypes (CD226$^+$, TIGIT$^+$, and CD226$^-$TIGIT$^-$), and each exhibited distinct gene expression signatures (Fig. 3G). Among them, CD226$^+$CCR7$^-$CD8$^+$ T cells expressed high levels of cytotoxic granular proteins such as Granulysin (GNLY), Granzyme B (GZMB), and Granzyme H (GZMH). While TIGIT$^+$CCR7$^-$CD8$^+$ T cells expressed high levels of class II major histocompatibility complex related-genes (*CD74*, *HLA-DRA*, and *HLA-DRB1*). CD155, as a common ligand of TIGIT and CD226, is mainly expressed in antigen presenting cells (APCs), especially monocytes and cDCs in our data set (supplementary Fig. 7A–B), and that the expression of CD155 on monocytes of patients in the PR period is significantly lower than that of newly diagnosed patients (supplementary Fig. 7C–J).

To characterize the pathway activation features of CD8$^+$ T cell subclusters, AUCell and gene set enrichment analysis (GSEA) were utilized to identify functional differences in multiple pathways based on the differentially expressed genes (DEGs) between the CD226$^+$ and TIGIT$^+$CCR7$^-$CD8$^+$ T cells. The AUCell results suggested that CD226$^+$CCR7$^-$CD8$^+$ T cells had enhanced adhesive and cytotoxic functions (supplementary Fig. 9A, B). Using external data (GSE10239, GSE9650 and GSE22443), we found that the down-regulated genes in the CD226$^+$CCR7$^-$CD8$^+$ T cells were concentrated in the sets of highly up-regulated genes derived from naive or memory CD8$^+$ T cells when compared to effector cells (Fig. 3H). Similarly, the highly expressed genes of the TIGIT$^+$CCR7$^-$CD8$^+$ T cells were concentrated in the sets of highly up-regulated genes derived from PD-1$^+$CD8$^+$ T cells when compared to the PD-1$^-$ cells (GSE26495) (Fig. 3H). These results suggested that CD226$^+$CCR7$^-$CD8$^+$ T cells were more likely to have the characteristics of highly activated effector CD8$^+$ T cells, while TIGIT$^+$CCR7$^-$CD8$^+$ T cells had characteristics similar to PD-1$^+$CD8$^+$ T cells.

Cohort validation and functional assays confirmed the alterations of TIGIT$^+$CCR7$^-$ Tregs in different stages of T1D

To validate the scRNA-seq results, in an independent cohort, flow cytometry (FCM) was performed using cell surface markers for the different clusters (supplementary Fig. 8A). All 125 cases in the cohort (supplementary Table. 3&4) were divided into four groups: HD ($n = 35$), new-onset T1D (n = 21), T1D in PR ($n = 34$, 0.85 ± 0.66 months after the onset of PR), and post-PR T1D patients ($n = 35$, 11.54 ± 8.47 months after PR ended). We performed a sample size calculation using PASS 15 software (NCSS, Kaysville, UT, USA), with $\alpha = 0.05$ and $1-\beta = 0.8$, which indicated a required sample size of 16 individuals per group (Cohort II). Our actual sample size has exceeded expectations. Compared with that of the HD (22.6 ± 6.2%), the proportion of TIGIT$^+$CCR7$^-$ Tregs decreased in new-onset patients (14.2 ± 7.5%), significantly increased in patients during PR (20.5 ± 4.9%), and then declined to a lower level in post-PR patients (14.0 ± 5.1%) (Fig. 4A), while the percentage of TIGIT$^-$CCR7$^+$ Tregs showed the opposite pattern during T1D progression (Fig. 4B). These results from the validation cohort were in line with those derived from the scRNA-seq analysis. Notably, there was a significant positive correlation between the percentage of TIGIT$^+$CCR7$^-$ Tregs and β-cell function (i.e., 2-hour postprandial C-peptide, PCP) ($R = 0.52$, $P < 0.001$, Fig. 4C). In contrast, TIGIT$^-$CCR7$^+$ Tregs were negatively correlated with β-cell function ($R = -0.44$, $P < 0.001$, Fig. 4D). To rule out any confounding effects of blood glucose on the Tregs, the proportion of TIGIT$^+$CCR7$^-$ and TIGIT$^-$CCR7$^+$ Tregs were measured in two groups of type 2 diabetes (T2D) individuals with different glycemic controls. No statistical differences in the TIGIT$^+$CCR7$^-$ and TIGIT$^-$CCR7$^+$ Tregs were identified between the glycated hemoglobin (HbA1c) < 7.5% (n = 11) and HbA1c ≥ 7.5% (n = 11) T2D subgroups (supplementary Fig. 8B).

To characterize the homeostatic and functional properties of Treg subsets, FCM was utilized, and the functional markers was assessed in an additional cohort comprising 40 T1D patients and 14 HD. When compared with TIGIT$^-$CCR7$^+$ Tregs, the TIGIT$^+$CCR7$^-$ Treg population demonstrated elevated FOXP3 (Fig. 4F). In alignment with pathway activity analysis, TIGIT$^+$CCR7$^-$ Tregs were found to secrete significantly greater levels of IL-10 (Fig. 4E), granzyme B (Fig. 4G), and TGF-β1 (Fig. 4H) than their TIGIT$^-$CCR7$^+$ counterparts. To evaluate the suppressive capabilities of these Treg subsets on CD8$^+$ T cell proliferation, TIGIT$^+$CCR7$^-$ and TIGIT$^-$CCR7$^+$ Tregs were isolated (supplementary Fig. 8C), and co-cultured with carboxyfluorescein diacetate succinimidyl ester (CFSE) labeled CD8$^+$ T cells at various ratios (0:1, 1:1, 1:2, 1:4, and 1:8) for a period of 72 hours. The TIGIT$^+$CCR7$^-$ Tregs demonstrated a more potent immunosuppressive effect on the CD8$^+$ T cells, as evidenced by the reduced proliferation in the CD8$^+$ T cells (Fig. 4I, supplementary Fig. 8D).

Cohort validation and functional assays confirmed the alterations of CD226$^+$CCR7$^-$CD8$^+$ T cells in different stages of T1D

To explore the proportional changes in the peripheral CD226$^+$ and TIGIT$^+$CCR7$^-$CD8$^+$ T cell subsets, we performed FCM (supplementary Fig. 9C) in the same cohort mentioned above (125 cases, 4 groups). Compared to the HD group (57.0 ± 5.9 %), the CD226$^+$CCR7$^-$CD8$^+$ T cell

https://doi.org/10.1038/s41467-024-53264-8

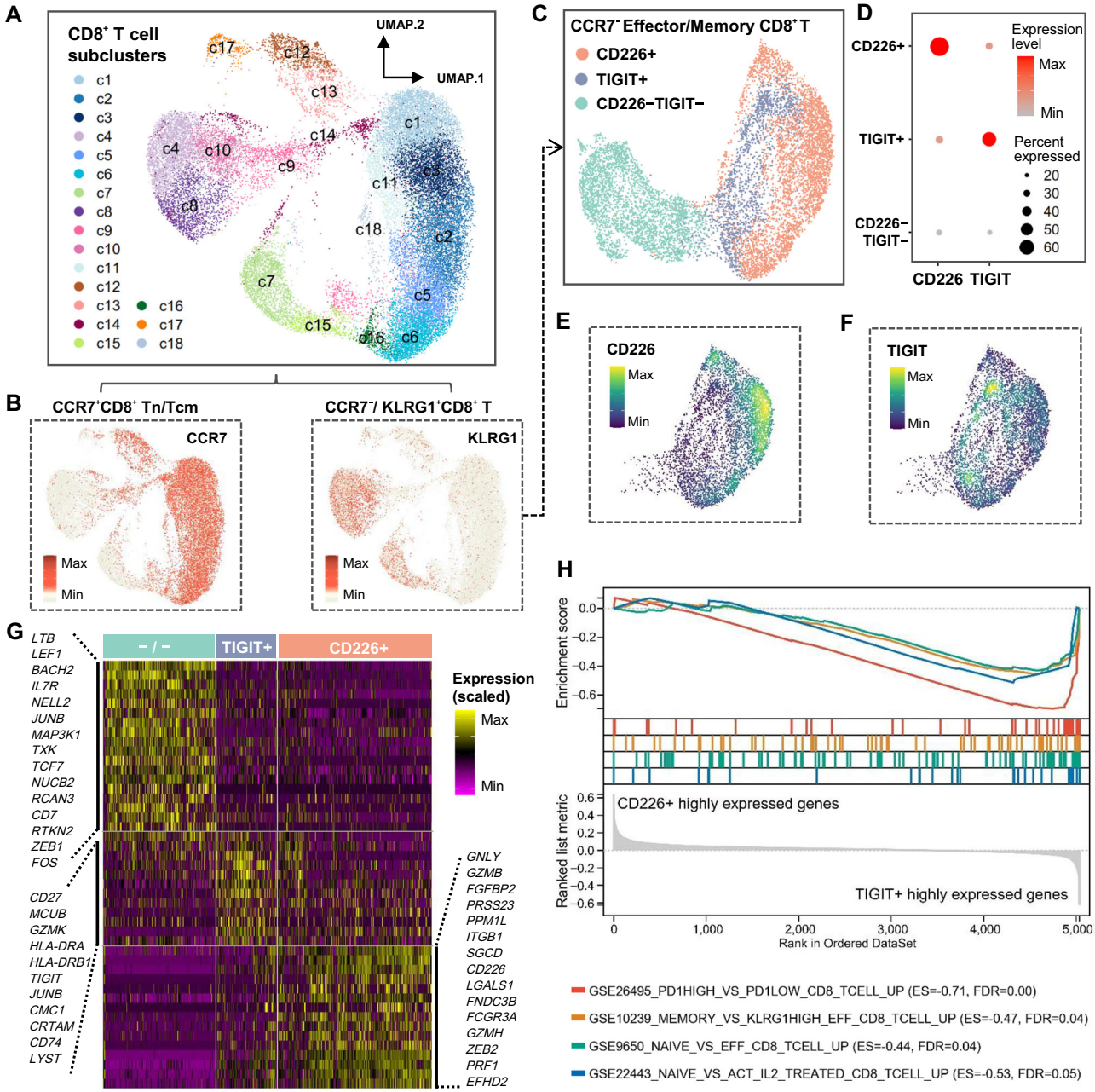

Fig. 3 | Dynamic changes in the composition and differentiation trajectories of circulating CD8⁺ T cells in different T1D phases. A UMAP visualization of CD8⁺ T cell subclusters. **B** UMAP plots showing the expression levels of CCR7 and KLRG1 in the CD8⁺ T subclusters. **C** UMAP plot representing 3 CCR7⁻CD8⁺ T cell phenotypes generated by re-annotation. **D** Dot plot showing the expression levels of CD226 and TIGIT in each CCR7⁻CD8⁺ T phenotype. The dot size was proportional to the percentage of gene expression. The dot colors indicate the scaled mean expression level. **E**, **F** UMAP plots representing the expression levels of CD226 and TIGIT in corresponding CCR7⁻CD8⁺ T subclusters. The visualization was generated using Nebulosa's kernel function. **G** Heatmap showing the scaled expression of the top DEGs among the 3 phenotypes. **H** GSEA analysis of the significant DEGs between CD226⁺ and TIGIT⁺CCR7⁻CD8⁺ T cells. Ranking of the DEGs is based on the fold difference. External gene sets were obtained from the GEO database. An enrichment score (ES) > 0 indicated that the pathway was upregulated in CD226⁺CCR7⁻CD8⁺ T cells, while an ES < 0 indicated that the pathway was upregulated in TIGIT⁺CCR7⁻CD8⁺ T cells. An FDR ˂0.05 was considered statistically significant.T1D, type 1 diabetes. Source data are provided as a Source Data File.

frequencies were increased among the CD8⁺ T cells in the new-onset patients (67.0 ± 6.8 %), significantly decreased in patients during PR (57.0 ± 7.9 %), and enriched to a high level in the post-PR patients (70.8 ± 6.6 %) (Fig. 5A), showing that there was a dynamic change pattern during the peri-PR phase. The percentage changes of the TIGIT⁺CCR7⁻CD8⁺ T cells around the peri-PR phase showed the opposing pattern (Fig. 5B). Notably, β-cell function assessed by PCP was negatively correlated with the percentage of CD226⁺CCR7⁻CD8⁺ T cells ($R = -0.66$, $P < 0.001$; Fig. 5C), and positively correlated with TIGIT⁺CCR7⁻CD8⁺ T cells ($R = 0.36$, $P = 0.0011$; Fig. 5D). To rule out any potential confounding effects imposed by hyperglycemia, the CD226⁺ and TIGIT⁺CCR7⁻CD8⁺ T cell subsets were identified in two groups of T2D populations: HbA1c < 7.5% ($n = 11$) and HbA1c ≥ 7.5% ($n = 11$). No statistical differences in the CD226⁺ and TIGIT⁺CCR7⁻CD8⁺ T cell subsets were identified between the two groups (supplementary Fig. 9D).

To further determine the phenotypic and functional characteristics of the CD8⁺ T cell subsets, FCM and functional assays were conducted using the same cohort of 40 patients with T1D and 14 HD

https://doi.org/10.1038/s41467-024-53264-8

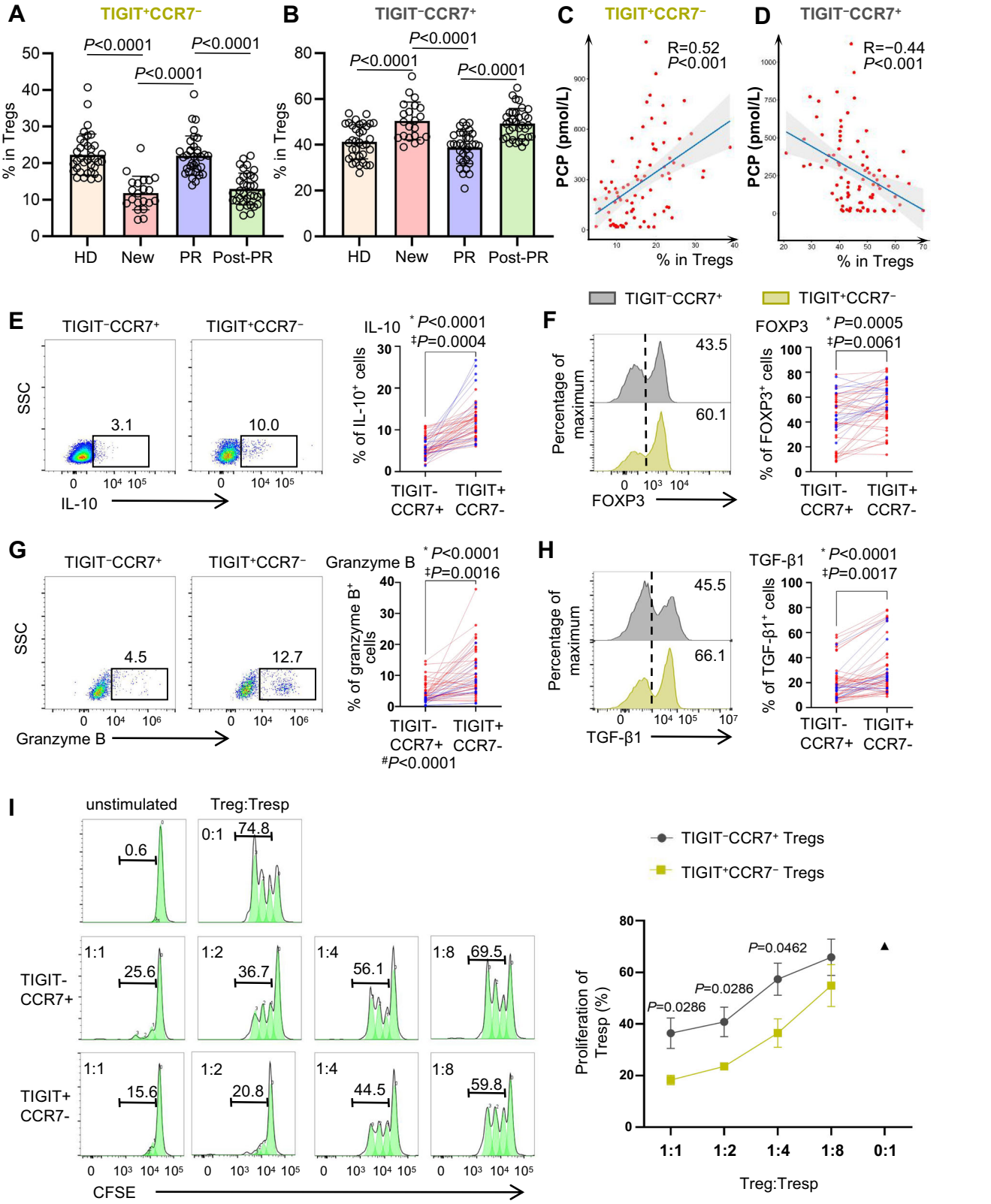

(Fig. 5E–J). The CD226$^+$CCR7$^-$CD8$^+$ T cells expressed different levels of the CTLA4, CD127, and CD62L proteins when compared to the TIGIT$^+$CCR7$^-$CD8$^+$ T cells (Fig. 5E–G). In line with pathway activity analysis, cytokine staining showed that CD226$^+$CCR7$^-$CD8$^+$ T cells secreted significantly higher amounts of perforin, GZMB, and proinflammatory cytokine tumor necrosis factor (TNF) when compared with the TIGIT$^+$CCR7$^-$CD8$^+$ T cells (Fig. 5H–J). For the assessment of cytotoxic activity, CD226$^+$ and TIGIT$^+$CD8$^+$ T cell subsets were isolated, and subsequently co-cultured with P815 mastocytoma cells for a duration of 5 hours to evaluate the induction of apoptosis in the target cells. CD226$^+$CD8$^+$ T cells exerted a significantly greater cytotoxic effect on P815 cells when compared to TIGIT$^+$CD8$^+$ T cells, as indicated by an increased rate of apoptosis in the P815 cells (Fig. 5K, L, supplementary Fig. 9E).

Fig. 4 | Changes in the composition and function of two distinctive Treg subsets. A, B Comparisons of the (**A**) TIGIT$^+$CCR7$^-$ and (**B**) TIGIT$^-$CCR7$^+$ Treg frequencies in the HD (n = 35), new-onset T1D (n = 21), T1D in PR (n = 34), and T1D post-PR (n = 35) groups. **C, D** Correlation analysis of the PCP levels with (**C**) TIGIT$^+$CCR7$^-$ and (**D**) TIGIT$^-$CCR7$^+$. P values were calculated using Spearman's correlation analysis. **E–H** Representative diagrams and quantification of (**E**) IL-10, (**F**) FOXP3, (**G**) granzyme B, and (**H**) TGF-β1 in TIGIT$^-$CCR7$^+$ and TIGIT$^+$CCR7$^-$ Tregs from T1D patients (red line, n = 40) and HD (blue line, n = 14). P values were calculated using a paired/unpaired two-tailed t-test, and data are presented as mean ± SD. '*' and '‡' denote statistical significance within T1D and HDs, respectively, between TIGIT$^-$CCR7$^+$ and TIGIT$^+$CCR7$^-$ Treg subpopulations; '#' signify statistical significance of marker expression in TIGIT$^-$CCR7$^+$ between T1D and HDs. **I** TIGIT$^+$CCR7$^-$ and TIGIT$^-$CCR7$^+$ Tregs, isolated from T1D patients (n = 4), were cocultured with CFSE labeled CD8$^+$ T cells in the presence of α-CD3/CD28 antibodies (0.5 bead/cell) for 72 h at 37 °C. The proliferation of CD8$^+$ T cells was measured. Two-tailed t-test; data are shown as the mean ± SEM. T1D, type 1 diabetes; NEW, new-onset; PR, partial remission; HD, healthy donor; PCP, postprandial C-peptide. n indicates the number of biologically independent samples examined. Source data are provided as a Source Data File.

Predictive value of CD226 and TIGIT-associated T-cell subsets for β-cell function declination in T1D

To further explore the potential of CD226 and TIGIT-related T cells as the predictive indicators for the β-cell function declination in T1D patients, we incorporated a cohort of 100 T1D patients who were diagnosed within six months of disease onset, and followed up at three-month intervals over a period of 24 months (Fig. 6A and supplementary Table. 5). The predictive variable was bifurcated into two outcome categories: patients who exhibited faster declination in their C-peptide area under the curve (CP-AUC) value (more than 50% decline relative to their baseline) were classified into the 'Fast' group, whereas those with a decline of less than 50% were classified into the 'Slow' group (Fig. 6B–D). By employing supervised machine learning classification algorithms, the support vector machines (SVM) model demonstrated notable performance (average AUC of 0.77 in internal validion cohort) in forecasting the rate of β-cell function deterioration in T1D patients (Fig. 6E, F). In external validation cohort, the model had mean AUC of 0.81, performing close to the internal validation (Fig. 6G). This suggested that CD226-related T cell subsets could partially predict the rate of islet failure in the early stage of T1D. An assessment of the importance of the independent variables showed that CD226-related immune signatures had a more important predictive role in this model (Fig. 6H).

Further, we explored the prognostic potential of TIGIT-associated Treg subsets in additional cohorts with similar methods (supplementary Fig. 10A, B). The results showed that the classifier constructed by the CatBoost algorithm could distinguish rapid progressors of islet function with a good performance of an average AUC of 0.73 with TIGIT$^+$CCR7$^-$ Tregs (supplementary Fig. 10C–E).

Interactions between CD226$^+$CCR7$^-$CD8$^+$ T cells and TIGIT$^+$CCR7$^-$ Tregs via TGF-β-mediated pathway

In light of the pronounced alterations observed in TIGIT$^+$CCR7$^-$ Tregs and CD226$^+$CCR7$^-$CD8$^+$ T cells across different stages of T1D, we investigated the cellular interactions between these subsets to elucidate the regulatory role of Tregs on CD8$^+$ T cell function. CellChat analysis revealed that TIGIT$^+$CCR7$^-$ Tregs emit a potent immunosuppressive TGF-β signal that specifically targets CD226$^+$CCR7$^-$CD8$^+$ T cells (Fig. 7A). Subsequent anlysis pinpointed the involvement of distinct TGF-β receptors, including TGF-β receptor type I (TGFBR1), type II (TGFBR2), and activin receptors type I (ACVR1) and type II (ACVR2), in mediating this signal to the CD226$^+$CCR7$^-$CD8$^+$ T cell subset (Fig. 7B).

Further serum analysis using enzyme-linked immunosorbent assay (ELISA) in T1D patients revealed a parallel relationship between TGF-β1 level fluctuations during the peri-PR phase and the dynamics of TIGIT$^+$CCR7$^-$ Tregs (Fig. 7C). Analysis of the supernatants from TIGIT$^+$CCR7$^-$ Treg cultures confirmed that these cells secreted higher TGF-β1 than TIGIT$^-$CCR7$^+$ Tregs (Fig. 7D). Additionally, we established that TGF-β1 intervention significantly inhibited the functional activity of CD226$^+$CCR7$^-$CD8$^+$ T cells in vitro (Fig. 7E, F). Crucially, co-culture experiments of TIGIT$^+$CCR7$^-$ Tregs with CD226$^+$CCR7$^-$CD8$^+$ T cells allowed for direct observation of the suppressive effect of TIGIT$^+$CCR7$^-$ Tregs on this particular CD8$^+$ T cell subset (Fig. 7G–I).

Alterations of TIGIT$^+$CCR7$^-$ Tregs and CD226$^+$CCR7$^-$CD8$^+$ T cells in NOD mice mirror the severity of insulitis

To explore the relationship between TIGIT$^+$CCR7$^-$ Tregs and CD226$^+$CCR7$^-$CD8$^+$ T cells with the severity of insulitis, we assessed these specific cellular subpopulations in the spleens and PLNs of NOD mice across the diasese course(supplementary Fig. 11A). In comparison to C57BL/6 mice, the splenic and PLN TIGIT$^+$CCR7$^-$ Treg cell proportions displayed a significant reduction, gradually declining in NOD mice at 4 weeks, 8 weeks, and 12 weeks of age (supplementary Fig. 11B). In contrast, the proportions of CD226$^+$CCR7$^-$CD8$^+$ T cells in the spleen and PLN were notably higher in NOD mice than in control C57BL/6 mice, progressively increased at 4 weeks, 8 weeks, and 12 weeks of age (supplementary Fig. 11C). The hematoxylin and eosin (H&E)-stained histological sections of pancreas tissues and correlation analysis revealed that these two cell types exhibited inverse ($r = -0.48$, $p = 0.014$ in the spleen; $r = -0.59$, $p = 0.005$ in PLN) and positive ($r = 0.60$, $p = 0.000$ in the spleen; $r = 0.48$, $p = 0.038$ in PLN) correlations, respectively, with the severity of insulitis (supplementary Fig. 11D–E). We also compared the association of TIGIT$^+$CCR7$^-$ Treg versus TIGIT$^-$CCR7$^+$ Treg with the severity of insulitis (supplementary Fig. 12).

Using multiplex fluorescence immunohistochemistry, we observed a substantial enrichment of the CD226$^+$CD8$^+$ T cell subset within infiltrating lymphocytes in severely damaged pancreatic islet tissues (supplementary Fig. 13A–C). We further performed bulk RNA sequencing of TIGIT$^+$ and CD226$^+$CD8$^+$ T cells, isolated from 8 NOD mice. This revealed differential expression of 4937 genes between the two populations, with a false discovery rate (FDR)-adjusted P value < 0.05 and log2-transformed fold change (log2FC) > 1 (supplementary Fig. 13D). Complementary to our previous functional experimental results, the CD226$^+$ subset, in contrast to TIGIT$^+$ cells, demonstrated enhanced cytokine secretion capabilities (supplementary Fig. 13E, F).

Anti-CD226 therapy inhibited the activation of CD8$^+$ T cells and alleviated hyperglycemia in vivo

We first assessed the binding efficiency (supplementary Fig. 14A) and validated the blocking effect of anti-CD226 monoclonal antibody (mAb) in vitro. CD8$^+$ T cells, isolated from the spleens of NOD mice, were cultured and exposed to anti-CD3 (5 μg/mL) and mPVR-Fc (5 μg/mL), either alone or in combination with anti-CD226 mAb (5 μg/mL), for a period of 24 h. It showed that CD226 blockade significantly suppressed both cell proliferation and cytokine production (supplementary Fig. 14B–D). To further elucidate the potential mechanistic action of anti-CD226 mAb, we evaluated the phosphorylation levels of signaling proteins within CD8$^+$ T cells post-CD226 blockade. Our results demonstrated a marked decrease in the phosphorylation of AKT and m-TOR proteins (supplementary Fig. 14E–G). These experiments confirmed that anti-CD226 mAb impaired CD8$^+$ T cell functionality through the inhibition of AKT-mTOR signaling pathway.

Furthermore, to demonstrate the prophylactic potential of the anti-CD226 mAb in T1D, we employed both the Cy-accelerated NOD and STZ-induced diabetic mouse models, with detailed experimental protocols outlined in Figs. 8A and 8G. Administration of the anti-CD226 mAb mitigated symptoms of diabetes in STZ-induced diabetic

https://doi.org/10.1038/s41467-024-53264-8

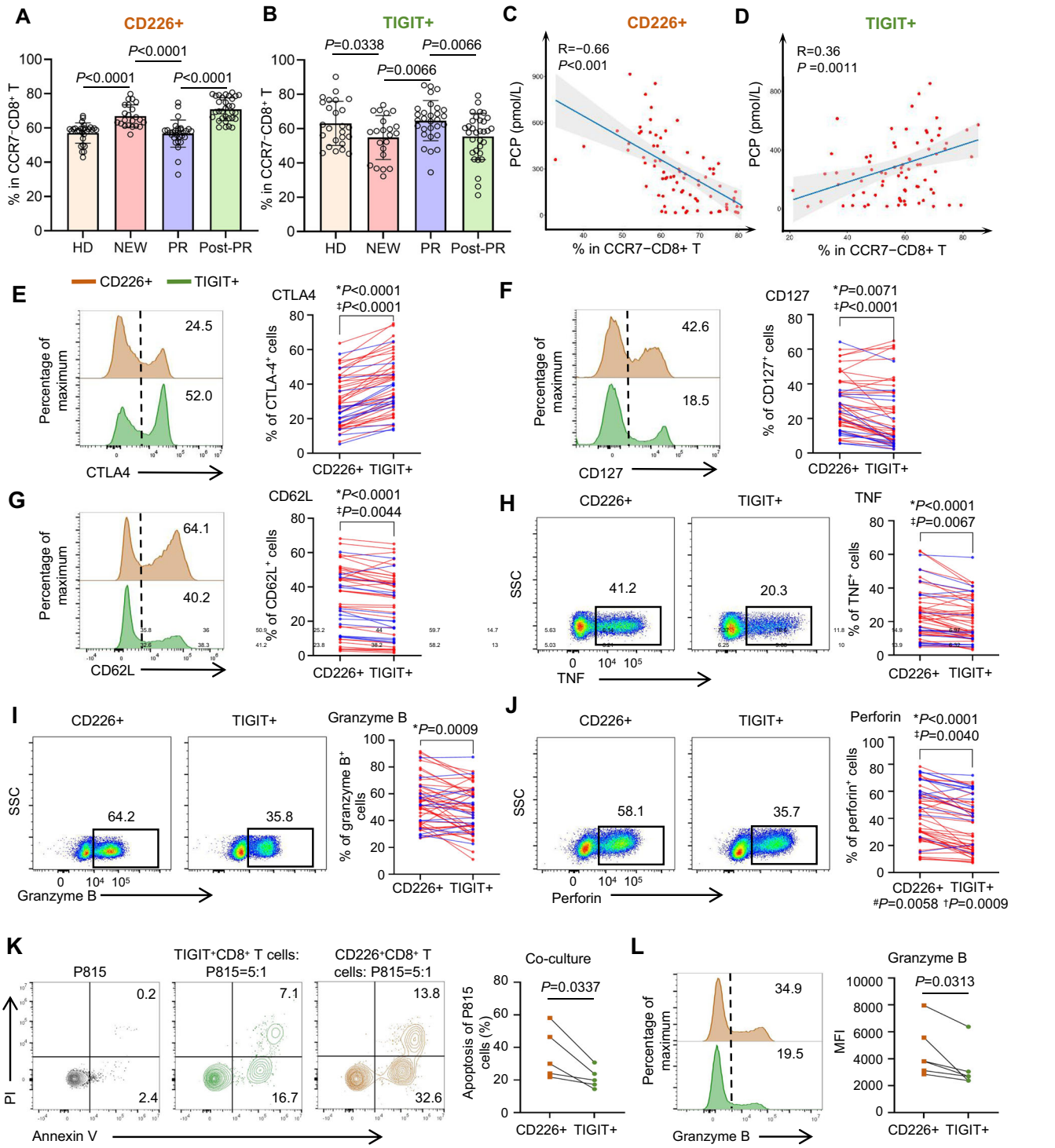

Fig. 5 | Changes in the composition and function between two T1D-stage-associated CD8⁺ T subsets. A, **B** Comparison of the (**A**) CD226⁺ and (**B**) TIGIT⁺CCR7⁻CD8⁺ T cell frequencies in the HD ($n = 35$), new-onset ($n = 21$), T1D in PR ($n = 34$), and post-PR T1D ($n = 35$) groups. **C**, **D** Correlation analysis of the PCP with (**C**) CD226⁺ and (**D**) TIGIT⁺CCR7⁻CD8⁺ T cells. *P* values were calculated using Spearman's correlation analysis. **E**–**J** Representative diagrams and quantification of (**E**) CTLA4, (**F**) CD127, (**G**) CD62L, (**H**) TNF, (**I**) granzyme B, and (**J**) perforin in CD226⁺ and TIGIT⁺CCR7⁻CD8⁺ T cells from T1D patients (red line, $n = 40$) and HD (blue line, $n = 14$). '*' and '‡' denote statistical significance within T1D and HDs, respectively, between CD226⁺ and TIGIT⁺CCR7⁻CD8⁺ T cell subpopulations; '#' and '†' signify statistical significance of marker expression in CD226⁺ and TIGIT⁺CCR7⁻CD8⁺ T cells, respectively, between T1D and HDs. **K**, **L** CD226⁺ and TIGIT⁺CD8⁺ T cells, isolated from T1D patients ($n = 6$), were cocultured with fluorescently labeled P815 cells at a ratio of 5:1 for 5 h at 37 °C. **K** Representative flow cytometry plots and quantification of apoptosis in P815 cells. **L** Representative peak plots and quantification of granzyme B expression within CD8⁺ T-cell subsets. *P* values were calculated using a paired/unpaired two-tailed t-test, and data are presented as mean ± SD. T1D, type 1 diabetes; NEW, new-onset; PR, partial remission; HD, healthy donor; PCP, postprandial C-peptide. n indicates the number of biologically independent samples examined. Source data are provided as a Source Data File.

https://doi.org/10.1038/s41467-024-53264-8

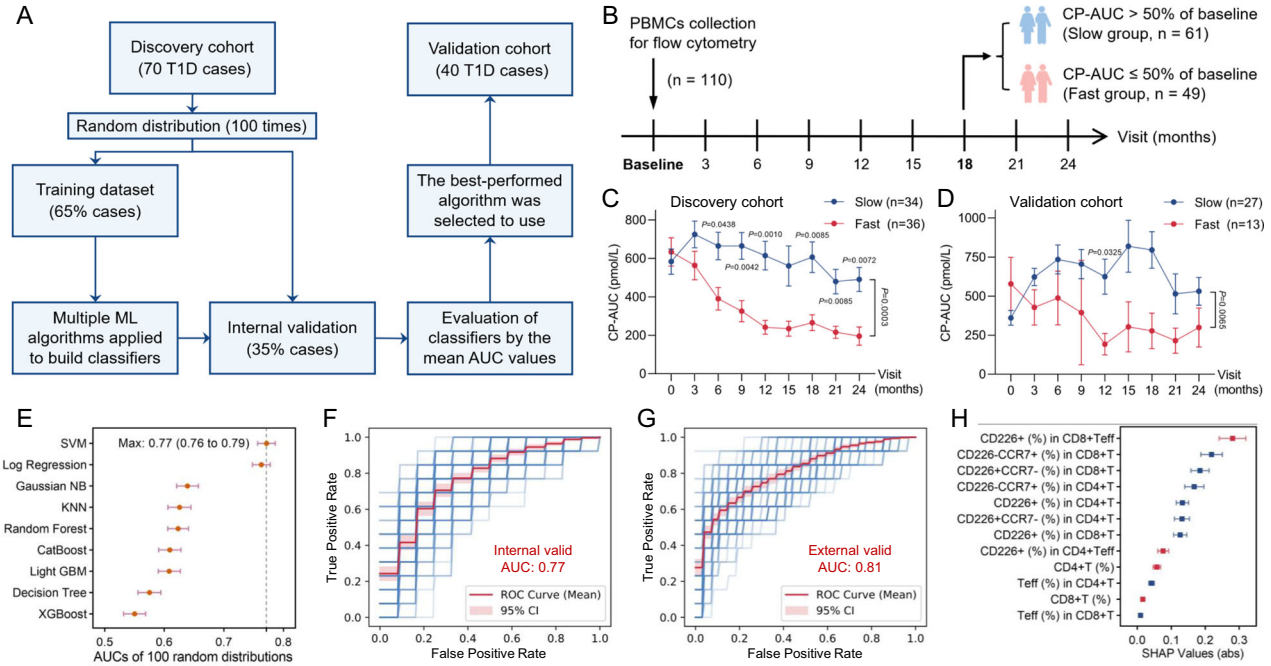

Fig. 6 | CellChat and machine learning revealed a role of CD226$^+$CCR7$^-$CD8$^+$ T cells in T1D progression. A Study design and cohort details for machine learning model development. **B** In the follow-up cohort, T1D patients were divided into 'Fast' and 'Slow' groups based on outcome events related to beta cell failure. **C**, **D** Temporal evolution of CP-AUC values in the discovery cohort and the external validation cohort of T1D patients. *P* were analyzed using mixed-effects model; data are shown as the mean ± SEM. **E** The comparative analysis of several machine learning algorithm models. AUC values derived from 100 random samplings are displayed for each model. Data are shown as the mean with 95% confidence interval. **F**, **G** The blue solid line shows the ROC curve of the SVM classifier over multiple random samples in the internal (**F**) or external (**G**) validation dataset. The red solid line represents the average ROC curve of all random sampling experiments, while the shaded area denotes the 95% confidence interval. **H** The mean absolute SHAP values for a particular feature across all samples assesses the average contribution of that feature. Each SHAP value is derived from each case in the training cohort ($n = 70$). Data are shown as the mean with 95% confidence interval. The higher the mean absolute SHAP value, the more significant the feature's contribution to the model prediction of the entire dataset. Positive SHAP values (shown in red) indicate that the feature has a positive impact on the model's predictions, and vice versa. T1D, type 1 diabetes; PBMCs, peripheral blood mononuclear cells; CP-AUC, C-peptide area under the curve. Source data are provided as a Source Data File.

mice, as indicated by reduced blood glucose levels (Fig. 8B) and enhanced glucose tolerance (supplementary Fig. 15A). Additionally, treatment with the anti-CD226 mAb resulted in decreased proliferation and cytokine production in both total (Fig. 8C–F) and CD226-expressing (supplementary Fig. 15B–F) CD8$^+$ T cells. Corresponding observations in the Cy-accelerated NOD model confirmed that blocking CD226 delayed the onset of T1D (Fig. 8H) and curtailed the activation of both total (Fig. 8I–L) and CD226-expressing (supplementary Fig. 16) CD8$^+$ T cells. Moreover, our results highlighted a critical role for the cellular equilibrium between CD226$^+$CD8$^+$ T cells and TIGIT$^+$ Tregs in both the STZ-induced (supplementary Fig. 17) and Cy-accelerated NOD (supplementary Fig. 18) mouse models.

Discussion

This study presents the first comprehensive single-cell resolution atlas of peripheral immune cells implicated in different stages (newly onset and PR pahse) of T1D. Following cohort verification and functional analysis, we identified TIGIT$^+$CCR7$^-$ Tregs, which exhibit potent immunosuppressive potential, were associated with PR stage and β-cell function, with their proportions declined in newly-diagnosed patients, increased during PR, and then decreased again after PR. In contrast, CD226$^+$CCR7$^-$CD8$^+$ T subsets, displaying a high cytotoxic potential and an inverse relationship with β-cell function, showed an opposing trend throughout disease progression. Machine learning models constructed using follow-up cohort data suggested that TIGIT$^+$CCR7$^-$ Tregs and CD226$^+$CCR7$^-$CD8$^+$ T cells held a significant predictive value for the progression of β-cell function in T1D. Further mechanistic data showed that TIGIT$^+$CCR7$^-$ Tregs may inhibit CD226$^+$CCR7$^-$CD8$^+$ T cells via TGF-β signaling. Notably, inhibition of CD226 effectively postponed the progression of insulitis, onset of diabetes, and ameliorated hyperglycemia in mouse models. Taken together, our data suggested an important role of the interplay between TIGIT$^+$CCR7$^-$ Tregs and CD226$^+$CCR7$^-$CD8$^+$ T cells in the pathogenesis of T1D (Fig. 9).

The critical role of Tregs in maintaining immune tolerance has long been recognized[28]. However, the frequency of Tregs is not always altered in autoimmune diseases including T1D[29]. Furthermore, exogenous repletion of the Tregs infusion when treating autoimmune diseases including T1D is not as satisfactory as was expected[28,30]. Therefore, it is important to investigate the heterogeneity and plasticity of Tregs and identify potential disease specific subsets. While there were no differences in the total number of Tregs in our T1D patients, we identified two Treg subsets specifically associated with β-cell function and T1D disease stage by scRNA-seq and cohort validation. The expansion of TIGIT$^+$CCR7$^-$ Tregs in the PR stage and decrease in new-onset and post-PR stages indicate that they may signature immunologic balance during the PR stage. Indeed, our findings revealed that the TIGIT$^+$CCR7$^-$ Tregs subset was characterized by elevated FOXP3 expression, enhanced TGF-β secretion, and a superior immunosuppressive function compared to the TIGIT$^-$CCR7$^+$ Tregs. The important role of TIGIT as a coinhibitory molecule in T cells has been recognized and TIGIT$^+$ Tregs are associated with the clinical outcomes of tumors such as melanoma[31], or autoimmune diseases such as systemic lupus erythematosus[32]. Interestingly, Tregs in the inflamed islets of NOD mice were found to be correlated with TIGIT expression in a previous study[33]. Our findings provided the first evidence of the association between the peripheral TIGIT$^+$CCR7$^-$ Tregs subset and the progression of T1D, demonstrating its potential as an

https://doi.org/10.1038/s41467-024-53264-8

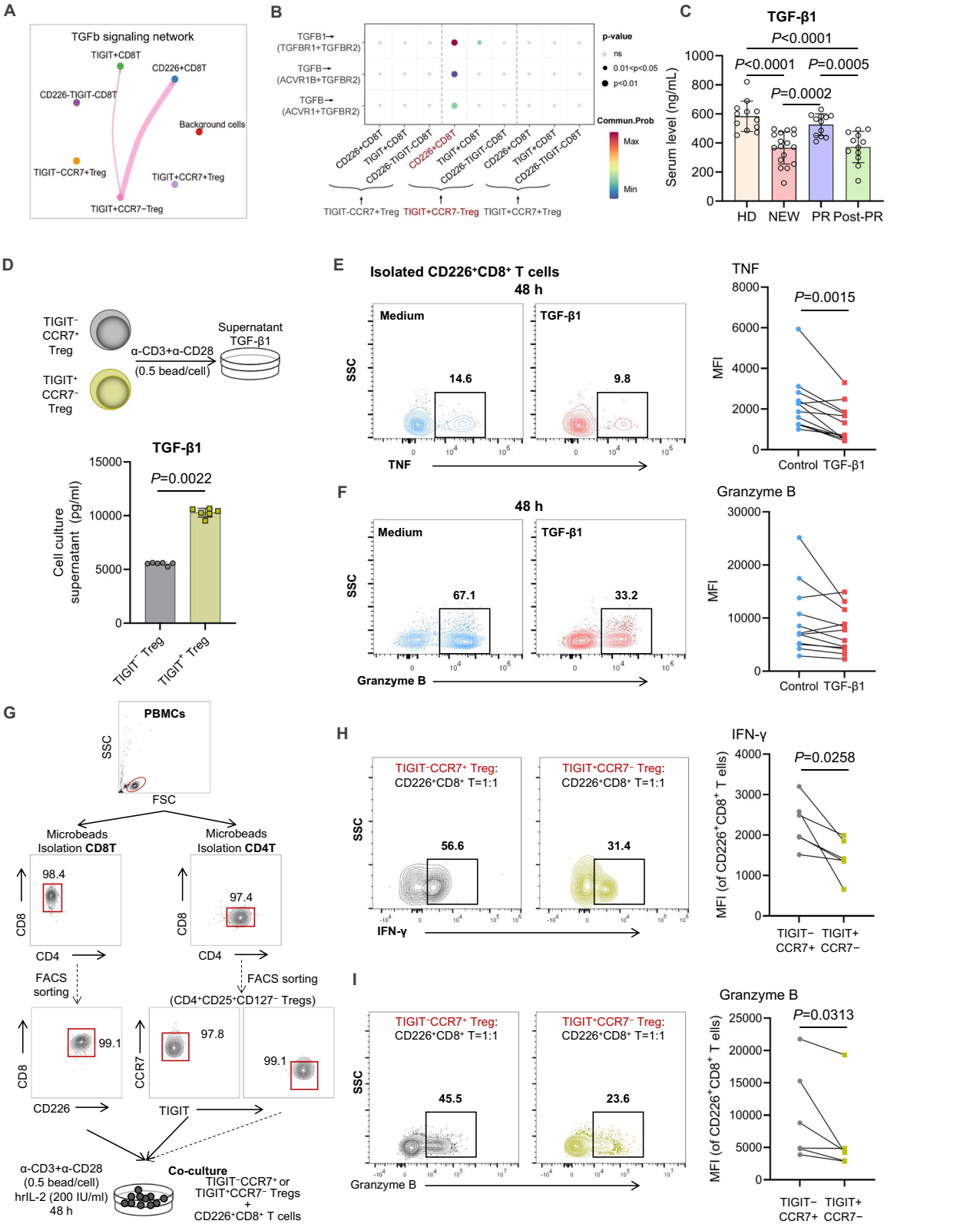

Fig. 7 | TIGIT⁺CCR7⁻ Tregs inhibit CD226⁺CCR7⁻CD8⁺ T cells via TGF-β1. A Circle plot showing the weight of TGF-β signaling interactions from the Treg to CD8⁺ T subclusters. **B** Dot plot representing the communications between the Treg (ligand provider) and CD8⁺ T cell subset. **C** Comparisons of the serum TGF-β1 levels in the HD ($n = 12$), new-onset T1D ($n = 17$), T1D in PR ($n = 12$), and T1D post-PR ($n = 12$) groups. **D** Sorted TIGIT⁺CCR7⁻ Treg and TIGIT⁻CCR7⁺ Treg from T1D patients ($n = 6$) were incubated with α-CD3/CD28 antibodies (0.5 bead/cell) for 48 h at 37 °C. The TGF-β1 levels in the supernatants were measured by ELISA. **E**, **F** Representative flow plots and expression levels of (**E**) TNF, and (**F**) granzyme B in CD226⁺CCR7⁻CD8⁺ T cells from T1D patients following 48 h of stimulation with or without 10 ng/ml TGF-β1 ($n = 12$). **G** Diagram illustrating the experimental setup. **H**, **I** Representative flow plots and expression levels of (**H**) IFN-γ, and (**I**) granzyme B in CD226⁺CCR7⁻CD8⁺ T cells from T1D patients following 48 h of co-culture with TIGIT⁺CCR7⁻ or TIGIT⁻CCR7⁺ Tregs at a 1:1 ratio ($n = 6$). Two-tailed paired/unpaired t-test; data are shown as the mean ± SD. T1D, type 1 diabetes; NEW, new-onset; PR, partial remission; HD, healthy donor; PBMCs, peripheral blood mononuclear cells. n indicates the number of biologically independent samples examined. Source data are provided as a Source Data File.

https://doi.org/10.1038/s41467-024-53264-8

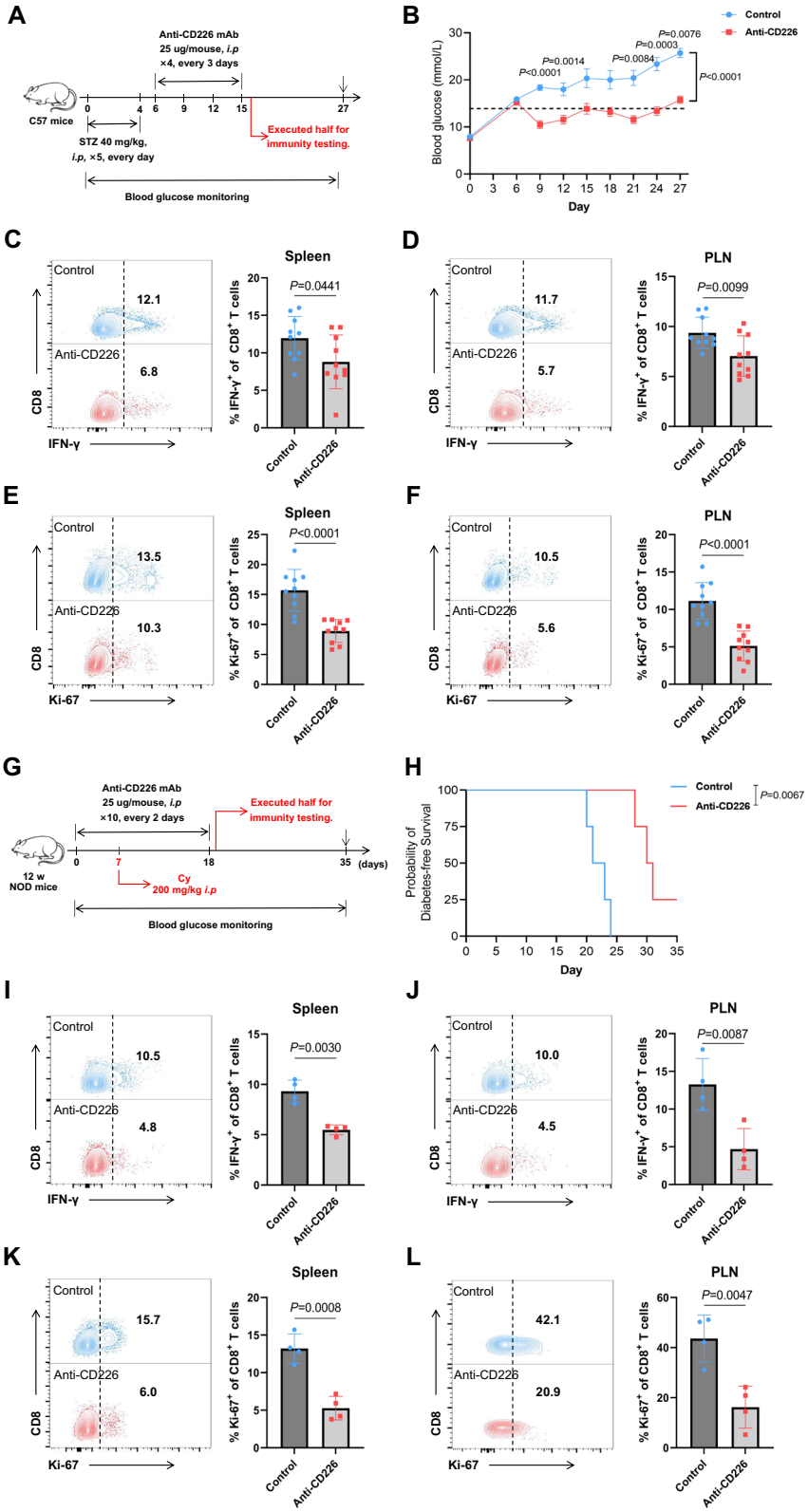

Fig. 8 | Anti-CD226 therapy inhibited the activation of CD8⁺ T cells and alleviated hyperglycemia in vivo. A–F Male C57BL/6 mice (n = 20/group) received STZ to induce diabetes. The Anti-CD226 group got 25 μg/mouse of the antibody every three days for four doses; controls had isotype injections. Post-treatment, five mice/group were analyzed for immune response; others were monitored for diabetes progression. **A** Experimental Design. **B** Non-fasting glucose levels ($n = 10$), analyzed using a mixed-effects model, data are shown as the mean ± SEM. **C–F** The expression levels of IFN-γ, and Ki-67 within CD8⁺ T cells in the spleen and PLN were depicted for the two groups ($n = 10$). **G–L** Female NOD mice (n = 8/group) received Cy to accelerate diabetes. After treatment with anti-CD226 or an isotype control, four were selected for immune profiling and the rest were monitored for diabetes onset. **G** Outlines of the protocol. **H** Survival curves indicating diabetes incidence ($n = 4$), analyzed by Log-rank test. **I–L** The expression levels of IFN-γ, and Ki-67 within CD8⁺ T cells in the spleen and PLN were shown (n = 4). *P* values were calculated using the unpaired two-tailed t-test; data are shown as the mean ± SD. T1D, type 1 diabetes; STZ, streptozotocin; PLN, pancreatic lymph nodes; Cy, cyclophosphamide. n indicates the number of biologically independent samples examined. Source data are provided as a Source Data File.

https://doi.org/10.1038/s41467-024-53264-8

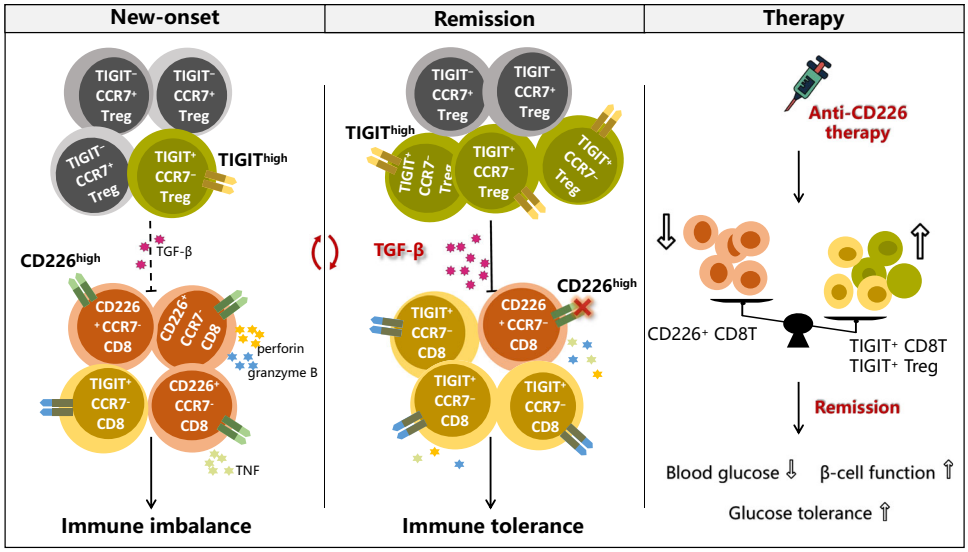

Fig. 9 | Model of immune perturbations characterized by TGF-β-modulated dynamic variability between TIGIT⁺CCR7⁻ Tregs and CD226⁺CCR7⁻CD8⁺ T cells for T1D onset and PR. T1D, type 1 diabetes; PR, partial remission.

effective predictor for islet function declination and promising disease-modifying therapies for T1D.

CD8⁺ T cells are responsible for directly destroying the islets of T1D patients[34]. Few studies have analyzed islet-infiltrating immune cells in patients with different stages of T1D due to their inaccessibility. It is therefore imperative to determine the comprehensive transcriptional profiles of CD8⁺ T cells in the peripheral blood of patients during different phases of T1D and identify the disease-related CD8⁺ T cell subsets. Our data showed that CD8⁺ T cells were dynamically changed along the disease stages and that the expression of CD226 and TIGIT was pivotal for distinguishing T1D-related CD8⁺ T subsets. Among classical effector CCR7⁻CD8⁺ T cells, the CD226⁺ subcluster was potentially more pathogenic; its proportion increased in new-onset T1D and was negatively correlated with islet function, while the TIGIT⁺ subcluster was the opposite. Phenotypic and functional analyses further highlighted the unique characteristics of these two subsets; notably, the CD226⁺ subset secreted significantly higher levels of perforin, GZMB, and the pro-inflammatory cytokine TNF, and exhibited increased cytotoxicity against target cells. These findings are consistent with previous studies[26,35,36]. Furthermore, using a follow-up cohort, we determined through machine learning algorithms that the proportion of circulating CD226⁺CCR7⁻CD8⁺ T cells had a high predictive performance for the pace of β-cell function decline in T1D patients.

The progression and PR of T1D are characterized by opposite alterations of TIGIT⁺CCR7⁻ Treg and CD226⁺CCR7⁻CD8⁺ T cell subsets. Our further cell-cell interaction analysis suggested that TIGIT⁺CCR7⁻ Tregs specifically inhibited CD226⁺CCR7⁻CD8⁺ T cells via the TGF-β signal. TGF-β could function as a suppressor to inhibit cytotoxic CD8⁺ T cell differentiation while promoting peripheral Tregs generation[37]. Moreover, we discovered that TGF-β1 levels in the serum of PR patients are higher than those in non-PR status. Hence, we speculated that the dynamics of TIGIT⁺CCR7⁻ Tregs/TFG-β/CD226⁺CCR7⁻CD8⁺ T cells were critical in T1D progression. Echoing this, Principe DR et al. reported that adoptive transfer of TGFBR-deficient CD8⁺ T cells promotes a cytotoxic response against tumors[38]. Our in vitro studies showed that TIGIT⁺ Tregs secreted higher levels of TGF-β1 compared to TIGIT⁻ Tregs, significantly inhibiting the activation of CD226⁺CD8⁺ T cells. Furthermore, the co-culture of TIGIT⁺ Treg cells with CD226⁺CD8⁺ T cells provided direct evidence of the inhibitory effect of TIGIT⁺ Tregs on CD226⁺CD8⁺ T cells. These results reveal for the first time that TIGIT⁺ Tregs may supress the activation of CD226⁺CD8⁺ T cells through the TGF-β1 signaling pathway. This interaction could play an important role in the re-establishment of immune tolerance during the PR phase of T1D.

Although promising, the protective effects of anti-CD3 mAbs on β-cell destruction in T1D are far from meeting the need to cure or prevent this disease. Should studies confirm that anti-CD226 mAbs effectively and safely modulate immune responses, they might have a synergenic impact on the basis of anti-CD3 mAbs in therapeutic potential. In this regard,it is intriguing to find that targeting CD226 could exert significant therapeutic effects in both the Cy-accelerated NOD and the STZ-induced diabetic mouse models, which shed light on the modulatory roles played by this costimulatory pathway in T1D. Further studies targeting at NOD model or pliot clinical trials could sure provide more solid evidence.

The treatment with anti-CD226 mAb led to a reduction in both proliferation and cytokine production of CD8⁺ T cells, consistent with existing literature[39]. Additionally, CD8⁺ T cells isolated from the spleens of NOD mice and treated in vitro with anti-CD3 and mPVR-Fc, either alone or in conjunction with anti-CD226 mAb, demonstrated substantial reductions in both cell proliferation and cytokine secretion, corroborating previous research[40]. Mechanistically, our findings indicated that inhibition of CD226 simultaneously suppressed the phosphorylation of AKT and mTOR, suggesting that anti-CD226 mAb may inhibit CD8⁺ T cell function by disrupting the AKT/mTOR signaling pathway. In this study, we sought to dissect the intricate balance between CD226⁺CD8⁺ T cells and TIGIT⁺CCR7⁻ Treg cells that orchestrates immune tolerance during the PR phase. To achieve this, we meticulously assessed the dynamic equilibrium of these two pivotal cell subpopulations in response to precise modulation with anti-CD226 therapeutic intervention.

Our study has a few limitations. First, the relatively small sample size included in scRNA-seq may have reduced the statistical power of the analysis. However, we verified our findings with a relatively adequate number of independent cohorts. Second, we focused on immune cells from circulating blood since it is challenging to obtain infiltrating immune cells in the pancreas during the course of T1D, and future studies of pancreatic lesions will help to further characterize the complex network of immune cells.

In conclusion, the results of this study provide a framework that will enrich our knowledge of the intricacies of T1D. Furthermore, the interplay identified between TIGIT⁺CCR7⁻ Tregs and CD226⁺CCR7⁻CD8⁺ T cells may offer mechanistic clues for therapeutic interventions.

However, maintaining the long-term effect of immunotherapy and preserving β-cell function by extending the PR phase is still a complex problem to overcome in the future.

Methods

Study cohort

Cohort I consisted of 9 T1D patients (5 new-onset and 4 in PR) and 3 HDs for single-cell sequencing. Cohort II consisted of 90 T1D patients at different stages (21 new-onset T1D, 34 T1D in PR, and 35 post-PR T1D patients) and 35 HDs for the in vitro validation experiments. Cohort III included 70 T1D patients who were followed up for 24 months for establishing predictive models with machine learning.

All patients with T1D were enrolled at the Second Xiangya Hospital of Central South University (Changsha, Hunan, China) from December 2020 to July 2022. The diagnosis of T1D was made according to the International Society for Pediatric and Adolescent Diabetes (ISPAD) guidelines[41] and our inclusion criteria were defined as follows: (i) insulin dependence from the time of disease onset, (ii) positivity for at least 1 of the 3 islet autoantibodies measured (glutamic acid decarboxylase antibody [GADA], insulinoma associated protein 2 antibody [IA-2A], and zinc transporter 8 antibody [ZnT8A]), (iii) disease duration of less than 2 years, and (iv) regular follow-up to measure fasting C-peptide (FCP), PCP, insulin dosage (INS dose), body mass index (BMI) or BMI z-score (BMI z), and HbA1c, enabling the identification of PR status.

HD were recruited through a recruitment advertisement at a local preschool education institution and local medical centers. All controls underwent oral glucose tolerance test (OGTT) screening, and their medical history was collected to exclude those with a positive family history of diabetes, infection, autoimmune disease, severe liver and kidney damage, or steroid hormone therapy. We also enrolled 20 T2D patients defined according to the American Diabetes Association (ADA) criteria with different blood glucose controls[42]: (i) HbA1c < 7.5% ($n = 11$), and (ii) HbA1c ≥ 7.5% ($n = 11$).

All participants, of Asian ethnicity, were drawn from various rural and urban regions throughout China. The sex of the study participants was determined through self-report during the initial demographic data collection. Informed consent was provided by all participants, and the study was approved by the Ethics Committee of the Second Xiangya Hospital of Central South University (SQ2016YFSF110035).

Definition of PR

The definition of PR in this study was based on either mixed meal tolerance test (MMTT)-stimulated C-peptide levels (≥ 300 pmol/L) or the index of insulin dose adjusted HbA1c (IDAA1c) (IDAA1C = HbA1c [%] + 4* daily insulin dose/kg ≤9). When C-peptide values were missing, IDAA1C values were used to define the PR, as previously reported[14]. Participants were classified into three subgroups according to their status: (i) patients with diabetes for less than 3 months who did not meet the definition of PR were classified as 'new-onset', (ii) patients currently in the PR stage were grouped into the 'PR' group, and (iii) patients whose PR phase had ended were defined as 'post-PR'.

C-peptide, HbA1c and islet autoantibodies assays

C-peptide levels were measured by a chemiluminescence method using the Advia Centaur System kit (Siemens, Munich, Germany). The inter- and intra-assay variation coefficients were 3.7% to 4.1% and 1.0% to 3.3%, respectively, as previously reported[43]. HbA1c was detected by automatic liquid chromatography (VARIANT II haemoglobin test system, Bio-Rad Laboratories, Hercules, CA, USA).

The determination of GADA, IA-2A, and ZnT8A was conducted through radioimmunoassay, as previously reported[44]. Samples that initially tested positive were re-evaluated with a second test to confirm their status. Only patients with confirmed positive results were included in the study. The sensitivities of the assays for GADA, IA-2A, and ZnT8A were found to be 82%, 76%, and 76%, respectively. Specificities reached 96.7%, 100%, and 100%, respectively, as determined by the Islet Autoantibody Standardization Program (IASP 2020).

Isolation and stimulation of peripheral blood mononuclear cells (PBMCs)

Fresh venous blood samples were drawn into sodium heparin tubes from fasting subjects and processed within two hours. PBMCs were isolated by standard Ficoll-Paque Plus density-gradient centrifugation.

scRNA-seq experiment

scRNA-seq was performed by CapitalBio Technology Inc. (Beijing, China). Cell density and survivability were evaluated in the fresh PBMCs from cohort I using Count Star (Alit life science, Shanghai, China), and the cell viability >90% for each sample. According to the manufacturer's instruction, single-cell suspensions were transformed to barcoded scRNA-seq libraries using a Chromium Single Cell B Chip Kit (10x Genomics, 1000074) and Single-cell 3′ Library and Gel Bead Kit V3 (10x Genomics, 1000075). Then, single-cell cDNA synthesis and amplification were generated in a S1000TM Touch Thermal Cycler (Bio Rad). Finally, the single-cell cDNA was sequenced on the Illumina NovaSeq 6000.

Quality control and data processing for scRNA-seq

Raw FASTQ files were mapped to human reference GRCh38 using 10X Genomics Cell Ranger software suite (https://support.10xgenomics.com/single-cell-gene-expression/software/downloads/latest)[45]. Fastq sequence quality filtering and sequencing alignment were performed sequentially using the Cell Ranger pipeline. The gene barcode matrix from all samples was then combined with the R package Seurat 3.0[46]. We performed the first round of filtering based on the conditions of removing genes detected in fewer than 3 cells and excluding cells with fewer than 200 detected genes. Subsequently, we applied scDblFinder for doublet detection. The criteria for inclusion in the second round of filtering include the number of genes between 200 and 6000, the total number of unique molecular identifier counts (UMI counts) ranging from 500 to 34000, and mitochondrial gene percentages below 13%. Following these steps, we initiated the clustering and manual annotations process on the overall cell population, guided by CellTypist's two models (supplementary Fig. 2) for major cell types. Notably, the second-round filtering already addressed the exclusion of a portion of doublets (supplementary Fig. 1), often characterized by exceptionally high UMI and gene counts. Subsequently, during annotation, we carefully detected and removed remaining doublets, informed by scDblFinder results, gene markers, and clustering outcomes. For major cell subgroups, as mentioned in the manuscript (e.g., $CD8^+$ T and $CD4^+$ T), we performed secondary clustering to refine immune phenotyping.

Perform dimensional reduction and clustering

A global-scaling normalization method 'LogNormalize' was employed to normalize the featured expression measurements for each cell by the total expression, and this was multiplied by a scale factor (10,000) and the result was log-transformed. A linear transformation (scaling) that was a standard pre-processing step prior to dimensional reduction techniques was then applied. The gene features that exhibited high cell-to-cell variation in the datasets were calculated using the function 'FindVariableFeatures'. Principal component analysis (PCA) was then conducted on the scaled variable features data. Prior to PCA for the overall PBMC cell subpopulations, the final number of Highly Variable Genes (HVGs) selected was set at 4000. In the subsequent round of clustering for specific cell types like $CD8^+$ T cells, 3000 HVGs were employed. The method for HVG selection used in FindVariableFeatures was the Variance Stabilizing Transformation (VST). Following PCA, the top 30 principal components were utilized for uniform manifold approximation and projection (UMAP), and graph-based clustering was performed with a resolution parameter set at 1.2. As with the clustering, a KNN graph based on the Euclidean distance in the

PCA space was utilized, and the edge weights were refined between any two cells based on the shared overlap in their local neighborhoods.

Batch effect correction

A multi-dataset integration algorithm 'Harmony' (https://github.com/immunogenomics/harmony) was used to correct the batch effect[47]. In brief, the batch effects were removed by the R package Harmony version 1.0 based on the top 50 PCA components identified. The batch variable used for correction was shown in supplementary Table. 1. All the analyses presented in this study were done on the Harmony corrected data.

Major cell type annotation

Cluster marker genes were recognized using the 'FindAllMarkers' function (supplementary Table. 2). Cell types were manually annotated guided by the results from CellTypist[48,49]. The CellTypist predictions were processed using the 'Healthy_COVID19_PBMC' and 'Immune_All_Low' models with majority voting classifiers. Monocytes, cDC, NK/NKT, $CD4^+$ T cells, $CD8^+$ T cells, and B cells were isolated from the whole scRNA-seq profile for a second round of re-clustering.

Detection of differentially expressed genes and functional enrichment analysis

Differential gene expression analysis for cell clusters was carried out in Seurat using the 'FindMarkers' function with the Wilcoxon test. This function was focusing on identifying DEGs between specific cell types or conditions. The P-values were adjusted using the Bonferroni correction. Pseudobulk analysis has been applied to identify differences between disease groups by the sample-level inferences[50]. The muscat R package was used to make pseudobulk analysis.

Pseudo-bulk analysis involved aggregating individual cell expressions at the sample level, and we utilized the sum aggregation method with default parameters. The DEGs were ranked by log2FC. GSEA was performed to enrich the biological function information of the DEGs[51]. Pathway-specific gene sets were downloaded from the GSEA database (http://www.gsea-msigdb.org/gsea). AUCell analysis was performed to evaluate pathway activity based on a given gene set[52]. AUCell is a ranking-based analysis that uses the 'AUC' to calculate whether a critical subset of the input gene set is enriched within the expressed genes for each cell.

Pseudotime analysis

Monocle3 was used to construct the pseudo-temporal trajectory inference[53,54]. Monocle3 modeled gene expression levels were based on pseudo-time values to show the variation of gene expression over the differentiation trajectories.

Inference of transcription factor regulatory network

SCENIC analysis was performed for simultaneous gene regulatory network reconstruction[52]. The SCENIC process involved: (1) identification of potential TF targets based on co-expression using GENIE3, (2) use of RcisTarget to determine direct targets (regulons), and (3) performing AUCell analysis to score the activity of the regulons on single cells.

Cell-cell interaction analysis

CellChat was utilized to investigate and visualize signaling pathway networks between different immune cells[55]. CellChat took gene expression data as the input and combined ligand-receptor pairs and their cofactor interactions to model cell-cell communication.

FCM

FCM was performed using standard surface and intracellular staining protocols. The antibody panels listed in supplementary Table 8. To identify the functions of the subset, PBMCs were stimulated for 4–6 hours using a lymphocyte activation cocktail (BD Bioscience, San Jose, CA, USA), which included phorbol myristate acetate (PMA), a calcium ionophore (Ionomycin), and the protein transport inhibitor BD GolgiPlug™ (Brefeldin A), in accordance with the manufacturer's recommendations. Following the surface staining cells were fixed and permeabilized using the Fixation/Permeabilization Buffer Kit (BD Biosciences) and further stained for intracellular cytokines and cytotoxic molecules. The analysis was performed using an LSR II instrument (BD Biosciences), and FlowJo 10.8.1 software (Treestar, San Carlos, CA, USA) was used to analyze the data.

Treg isolation and suppression assay

We initially purified $CD4^+$ T cells from T1D patients using anti-CD4 magnetic beads (Miltenyi Biotec, Bergisch Gladbach, Germany), followed by cell sorting of $TIGIT^+CCR7^-$ and $TIGIT^-CCR7^+$ Treg ($CD4^+CD25^+CD127^-$) subsets using the FACS Aria II cell sorter (BD Biosciences). The flow-sorted Treg subsets were then co-cultured in varying ratios (0:1, 1:1, 1:2, 1:4 and 1:8) with CFSE stained $CD8^+$ T cells, in Roswell Park Memorial Institute (RPMI)-1640 medium with 10% fetal bovine serum (FBS), 100 U/mL penicillin, and 100 mg/mL streptomycin (GenClone; Genesee Scientific) for 72 h at 37°C and 5% CO_2 in the presence of anti-human CD3/CD28-conjugated beads (0.5 bead/cell, ThermoFisher Scientific, Pittsburgh, PA, USA). Cell proliferation was analyzed by FCM using a LSR II (BD Biosciences).

Cytotoxicity assay

We initially used anti-CD8 magnetic beads (Miltenyi Biotec) to purify $CD8^+$ T cells from T1D patients, followed by cell sorting of $CD226^+$ and $TIGIT^+CD8^+$ T cells using the FACS Aria II cell sorter (BD Biosciences). P815 cells were labeled with 5 ul of 1,1'-Dioctadecyl-3,3,3',3'-Tetramethylindodicarbocyanine,4-Chlorobenzenesulfonate Salt (DiD') dye (V22887, ThermoFisher) per 10^6 cells for 15 min at 37 °C. $CD226^+$ and $TIGIT^+CD8^+$ T cells were incubated with these P815 cells in 96-well round-bottom plates for 5 h at 37 °C and 5% CO_2. Early (Annexin V positive; PI negative) and late apoptosis (Annexin V positive; PI positive) of P815 were detected at 5 h by FCM (Annexin V Apoptosis Detection Kit, ThermoFisher).

In vitro intervention of $CD226^+CD8^+$ T cells

To analyze the TGF-β-responsiveness of the T cells, $CD226^+CD8^+$ T cells were cultured in the presence of TGF-β (10 ng/ml; Peprotech, Rocky Hill, NJ, USA) for 48 h at 37 °C and 5% CO_2, and then stained for intracellular cytokines.

ELISA

Serum TGF-β levels were measured by ELISA using a human TGF-β ELISA kit (Novus Biologics, Littleton, CO, USA) according to the manufacturer's instructions. $TIGIT^+CCR7^-$ and $TIGIT^-CCR7^+$ Treg subsets were separately isolated and cultured with anti-human CD3/CD28-conjugated beads (0.5 bead/cell, ThermoFisher). The cell culture supernatants TGF-β levels were measured by ELISA after 48 h.

In vitro co-cultivation system

Utilizing the described methods, $TIGIT^+CCR7^-$ and $TIGIT^-CCR7^+$ Treg subsets, and $CD226^+CD8^+$ T cells were isolated and co-cultured in a 1:1 ratio in the presence of anti-human CD3/CD28-conjugated beads (0.5 bead/cell, ThermoFisher) and human recombinant IL-2 (hrIL-2, 200 IU/mL, Peprotech). The intracellular cytokines of the $CD226^+CD8^+$ T cells were then assessed after 48 h.

Construction and evaluation of machine learning model

We enrolled two cohorts comprising 110 T1D patients diagnosed within 6 months and conducted follow-up observations every three months over a 24-month period (supplementary Table 5–6). The discovery cohort consisted of 70 new-onset T1D patients and was mainly used to train the model. An independent validation cohort consisting of 40

patients was used as external validation of the model. The target predictive variables were categorized based on two outcome groups: patients with a decline in CP-AUC exceeding 50% from baseline at the 18-month follow-up were classified as the 'Fast' group, while those with a decline below 50% were categorized as the 'Slow' group.

To mitigate the potential impact of randomness on our results, we repeated the random sampling 100 times in the discovery cohort. In each iteration, the discovery cohort dataset was partitioned into a training dataset and internal validation dataset, with the internal validation comprising 35% of the total data. Different random seeds were employed in each random sampling iteration to ensure robustness. In each repetition, we trained multiple classifiers on the training set, utilizing the frequencies of target cell types (derived from flow cytometry) as features, with different outcome events ('Fast group' or 'Slow group') serving as the target variable. We employed the Python library Scikit-Learn to construct, train, and evaluate diverse machine-learning models for the purpose of addressing classification challenges. These models included K-Nearest-Neighbor (KNN), logistic regression, support vector machines (SVM), gaussian naive bayes (Gaussian NB), decision trees, and random forests. Additionally, we leveraged ensemble boosting classifier models, specifically extreme gradient boosting (XGBoost), light gradient boosting machine (Light GBM), and categorical boosting (CatBoost). Subsequently, predictions were made on the internal validation dataset using the trained models, yielding predicted probabilities. To evaluate the performance of our models, we calculated the mean of all 100 AUC values obtained from the random sampling. The AUC serves as a key performance metric, providing a comprehensive assessment of the classifiers' discriminative abilities across various data subsets. The best-performed algorithm model was selected and further used for prediction on the external validation.

SHAP (SHapley Additive exPlanations) provides insights into model predictions. For each sample, SHAP values signify the contribution of each feature to the prediction. By computing the mean absolute value of the SHAP values for a specific feature across all samples, we assess the feature's average contribution to the entire dataset. A higher mean absolute value of SHAP indicates a more significant contribution of that feature to the model's predictions across the dataset. Positive SHAP values (highlighted in red in Fig.6H) denote that the feature positively influences the model's predictions. In other words, an increase in the feature value tends to lead the model towards higher predictions, and vice versa.

Mice

Wild-type C57BL/6 mice (male, 6–8 weeks old; stock N000013) and NOD/ShiLtj mice (female, 4–6 weeks old; stock N000235) were purchased from GemPharmatech (JiangSu, China). All animals were housed in the specific pathogen-free (SPF) animal facility in a temperature (72 ± 3 °F)- and air (50 ± 20% relative humidity)-controlled room with a 12-h light/dark cycle and were given a standard diet and tap water. The experimental/control animals were bred separately. The mice were euthanized using carbon dioxide (CO2) inhalation to induce asphyxiation, followed by cervical dislocation as a secondary euthanasia. All animal experiments were conducted following protocols approved by the Institutional Animal Care and Use Committee of Central South University (protocol No. 2021sydw0252).

Histology and assessment of insulitis

Pancreatic samples were fixed in 4% formalin overnight and subsequently embedded in paraffin. Embedding, sectioning, and H&E staining procedures were conducted by Servicebio Company (Wuhan, China). The extent of insulitis was assessed using three non-sequential slides from 3 to 5 individual mice. Each islet on every section was assigned a score based on the following criteria: 0=no lymphocytic infiltration, 1=peri-insulitis (< 30% infiltration), 2 = < 50% islet infiltration, and 3 = > 50% islet infiltration.

Multi-color immunofluorescence

The multi-color immunofluorescence protocol was based on the tyramide signal amplification (TSA) system. Briefly, tissue sections were deparaffinized, rehydrated, and subjected to heating-induced epitope retrieval (HIER) followed by H2O2 and 3% BSA blocking to prevent nonspecific staining. Then, the sections were incubated with primary antibodies specific for CD4/CD8 or FOXP3/CD226 (Abcam, Cambridge, MA, USA), an HRP-conjugated anti-rabbit secondary antibody and fluorescent tyramide (Biotium, Fremont, CA, USA) successively. They were then subjected to HIER again, and the process from BSA blocking through another round of antibody staining was repeated; in the end, DAPI (Sigma-Aldrich, St. Louis, MO, USA) was added to stain the nuclei, and the sections were imaged by a fluorescence microscope (Nikon, Tokyo, Japan).

Bulk RNA-seq

We initially used anti-CD8 magnetic beads (Miltenyi Biotec) to purify $CD8^+$ T cells from NOD mice, followed by cell sorting of $CD226^+$ and $TIGIT^+$ subsets using the FACS Aria II cell sorter (BD Biosciences). Total RNA was extracted using Trizol reagent (Thermo Fisher) according to the manufacturer's procedure. RNA-sequencing was completed using Illumina Novaseq 6000 (LC-Bio Technology Co., Ltd., Hangzhou, China). Raw sequencing reads were first subjected to quality control using FastQC, to ensure data integrity. Clean reads were then aligned to the reference genome using the Spliced Transcripts Alignment to a Reference (STAR) aligner. Transcript abundance was quantified using featureCounts, which provides read counts for each gene. The read counts were normalized to account for library size and other technical variations using the DESeq2 package. Differential expression analysis was then performed to identify genes with statistically significant changes in expression between conditions. Among the eight samples, a minimum of a one-fold difference in log 2 expression and FDR-adjusted P value < 0.05 were considered as expression differences.

Induction and assessment of the STZ-induced diabetic mouse model

Diabetes was induced in male C57BL/6 mice, aged 6–8 weeks, by administering multiple low-dose injections of STZ (Sigma). STZ was dissolved in fresh cold 0.01 M citrate buffer (pH 4.5) and administered intraperitoneally at a dose of 40 mg/kg for 5 consecutive days. Mice were fasted for 4–6 hours prior to STZ injection, and overnight access to 10% sucrose water was provided after the first injection to prevent sudden hypoglycemia. Blood glucose concentrations exceeding 250 mg/dL or 13.9 mmol/L in two consecutive daily measurements were considered indicative of diabetes onset.

Anti-CD226 mAb (clone #: 10E5, Thermo Fisher) or isotype Rat IgG2b were administered via intraperitoneal (i.p.) injection at a dose of 25 μg per mouse on days 6, 9, 12, and 15. Following treatment, five mice per group were euthanized for immune analysis, and the rest later to gauge long-term therapy outcomes.

Induction and assessment of the NOD Cy-accelerated diabetic mouse model

NOD/ShiLtj mice (female, 12 weeks old) were administered a single Cy dose of 200 mg/kg intraperitoneally to precipitate diabetes on day 7. The Anti-CD226 group was treated with 25 μg of anti-CD226 mAb on days 0, 2, 4, 6, 8, 10, 12, 14, 16 and 18, while the control group received isotype injections. Four mice from each group were euthanized for immune profiling post-treatment, with the remainder observed subsequently to assess the diabetic incidence.

Mouse cell isolation and ex vivo culture

The spleens or PLN of mice were collected and processed to obtain single-cell suspensions using a 40-μm cell strainer (352340, Corning, USA). Splenic erythrocytes were lysed with a red blood cell lysis buffer

(SigmaAldrich, St. Louis, MO, USA), and T cells were enriched using nylon wool (18369-50, Polysciences, USA). Splenic $CD8^+$ T cells were enriched using anti-CD8 magnetic beads (Miltenyi Biotec) and cultured ex vivo at 37°C in 24-well U-bottom plates (2×10^5 cells/mL) in the presence of mPVR-Fc (5 μg/mL, Recombinant Mouse CD155/PVR Fc Chimera Protein, CF, R&D Systems), anti-CD3 (5 μg/mL, R&D Systems), and/or anti-CD226 (5 μg/mL, Thermo Fisher) antibodies as indicated for 24 h.

For rat antimouse CD226 mAb (10E5) binding assay, $2{\times}10^5$ splenic $CD8^+$ T cells were incubated with diferent concentrations of antibodies (10E5) and 5 μg/mL mPVR-hFc fusion protein. DyLight 488-conjugated goat anti-human IgG Fc antibody (ab98619, abcam, Cambridge, MA, USA) was used to detect the binding frequency of mPVR-Fc fusion protein.

Western blot analysis

Western blots (WBs) were performed according to the standard protocol. Briefly, Protein samples were subjected to SDS-PAGE gels, electrophoresed, transferred to polyvinylidene fluoride (PVDF) membranes (Bio-Rad, Hercules, CA, USA). The membranes were blocked in 5% non-fat milk for 30 min, and then incubated with primary antibodies [actin (ab8227, Abcam), AKT (ab8805, Abcam), p-AKT (ab38449, Abcam), mTOR (ab51089, Abcam), and p-mTOR (ab51044, Abcam)] at 4°C overnight. Membranes were then incubated with horseradish peroxidase (HRP)-conjugated secondary antibodies for another hour at room temperature and developed with an chemiluminescence kit (Bio-Rad). Signals were visualized using Chemidoc XRS + (Bio-Rad). The ImageJ 1.50i software (Wayne Rasband, National Institute of Health, USA) was used to quantify the WB results.

Statistical analysis

Data are expressed as mean ± standard deviation (SD) for normally distributed variables or as median with range (minimum–maximum) for non-normally distributed variables. Group comparisons were conducted using unpaired or paired Student's t-tests as appropriate. One-way ANOVA was utilized for between-group comparisons with adjustments for potential confounders such as age, gender, and BMI, where collinearity analysis revealed no significant interactions between these variables. For analyzing the time-dependent changes in CP-AUC values within the longitudinal T1D patient cohort, a mixed-effects model with Bonferroni correction for multiple comparisons was employed. The normality of data distribution was verified using the Kolmogorov–Smirnov test. Nonparametric tests, including the Wilcoxon test or Mann–Whitney U test, were applied to parameters with non-normal distributions. Pearson correlation analysis was employed for data that followed a normal distribution, while Spearman correlation analysis was utilized for data that did not adhere to normality. The log-rank test was applied for survival curve analysis. Statistical computations were performed using R software version 4.1.0 (R Core Team, Vienna, Austria), Python version 3.6 (Python Software Foundation, Beaverton, Oregon), SPSS version 25.0 (IBM Corporation, Chicago, IL), and GraphPad Prism version 9 (GraphPad Software, San Diego, CA). Significance was established at a two-tailed P-value of less than 0.05.

Reporting summary

Further information on research design is available in the Nature Portfolio Reporting Summary linked to this article.

Data availability

The scRNA-seq data generated in this study have been deposited in the NCBI Gene Expression Omnibus (GEO) database under accession code GSE221297. We confrm that our study is compliant with the Guidance of the Ministry of Science and Technology (MOST) for the Review and Approval of Human Genetic Resources. The data have been deposited in the OMIX, China National Center for Bioinformation/Beijing Institute of Genomics, Chinese Academy of Sciences (https://ngdc.cncb.ac.cn/omix/release/OMIX005173). Source data are provided with this paper.

Code availability

The code can be accessed at https://github.com/Lxy-xyeyy/scRNAseq-T1D.

References

1. Gregory, G. A. et al. Global incidence, prevalence, and mortality of type 1 diabetes in 2021 with projection to 2040: a modelling study. *Lancet Diab. Endocrinol.* **10**, 741–760 (2022).
2. Norris, J. M., Johnson, R. K. & Stene, L. C. Type 1 diabetes-early life origins and changing epidemiology. *Lancet Diab. Endocrinol.* **8**, 226–238 (2020).
3. Herold, K. C. et al. An Anti-CD3 Antibody, Teplizumab, in Relatives at Risk for Type 1 Diabetes. *N. Engl. J. Med.* **381**, 603–613 (2019).
4. Herold, K. C. et al. Teplizumab: A Disease-Modifying Therapy for Type 1 Diabetes That Preserves β-Cell Function. *Diabetes Care*, https://doi.org/10.2337/dc23-0675 (2023).
5. Beran, D. et al. Teplizumab approval for type 1 diabetes in the USA. *Lancet Diab. Endocrinol.* **11**, 78–80 (2023).
6. Dayan, C. M. et al. Preventing type 1 diabetes in childhood. *Science* **373**, 506–510 (2021).
7. Bluestone, J. A., Buckner, J. H. & Herold, K. C. Immunotherapy: Building a bridge to a cure for type 1 diabetes. *Science* **373**, 510–516 (2021).
8. Boldison, J. & Wong, F. S. Immune and Pancreatic β Cell Interactions in Type 1 Diabetes. *Trends Endocrinol. Metab.* **27**, 856–867 (2016).
9. Zakharov, P. N., Hu, H., Wan, X. & Unanue, E. R. Single-cell RNA sequencing of murine islets shows high cellular complexity at all stages of autoimmune diabetes. *J. Exp. Med.* **217**, https://doi.org/10.1084/jem.20192362 (2020).
10. Collier, J. L., Weiss, S. A., Pauken, K. E., Sen, D. R. & Sharpe, A. H. Not-so-opposite ends of the spectrum: CD8(+) T cell dysfunction across chronic infection, cancer and autoimmunity. *Nat. Immunol.* **22**, 809–819 (2021).
11. Hu, H., Zakharov, P. N., Peterson, O. J. & Unanue, E. R. Cytocidal macrophages in symbiosis with CD4 and CD8 T cells cause acute diabetes following checkpoint blockade of PD-1 in NOD mice. *Proc. Natl Acad. Sci. USA* **117**, 31319–31330 (2020).
12. Scherm, M. G. et al. miRNA142-3p targets Tet2 and impairs Treg differentiation and stability in models of type 1 diabetes. *Nat. Commun.* **10**, 5697 (2019).
13. Gearty, S. V. et al. An autoimmune stem-like CD8 T cell population drives type 1 diabetes. *Nature* **602**, 156–161 (2022).
14. Li, X. et al. PD-1 and PD-L1 Expression in Peripheral CD4/CD8+ T Cells Is Restored in the Partial Remission Phase in Type 1 Diabetes. *J. Clin. Endocrinol. Metab.* **105**, https://doi.org/10.1210/clinem/dgaa130 (2020).
15. Tang, R. et al. Enhanced T Cell Glucose Uptake Is Associated With Progression of Beta-Cell Function in Type 1 Diabetes. *Front Immunol.* **13**, 897047 (2022).
16. Tang, R., Zhong, T., Lei, K., Lin, X. & Li, X. Recovery of intracellular glucose uptake in T cells during partial remission of type 1 diabetes. *Diabetologia* **66**, 1532–1543 (2023).
17. Villalba, A. et al. Partial remission and early stages of pediatric type 1 diabetes display immunoregulatory changes. A pilot study. *Transl. Res* **210**, 8–25 (2019).
18. Moya, R. et al. A pilot study showing associations between frequency of CD4(+) memory cell subsets at diagnosis and duration of partial remission in type 1 diabetes. *Clin. Immunol.* **166-167**, 72–80 (2016).
19. Sun, L., Su, Y., Jiao, A., Wang, X. & Zhang, B. T cells in health and disease. *Signal Transduct. Target Ther.* **8**, 235 (2023).

20. ElTanbouly, M. A. & Noelle, R. J. Rethinking peripheral T cell tolerance: checkpoints across a T cell's journey. *Nat. Rev. Immunol.* **21**, 257–267 (2021).
21. McKinney, E. F., Lee, J. C., Jayne, D. R., Lyons, P. A. & Smith, K. G. T-cell exhaustion, co-stimulation and clinical outcome in autoimmunity and infection. *Nature* **523**, 612–616 (2015).
22. Linsley, P. S. & Long, S. A. Enforcing the checkpoints: harnessing T-cell exhaustion for therapy of T1D. *Curr. Opin. Endocrinol. Diab. Obes.* **26**, 213–218 (2019).
23. Joller, N. et al. Treg cells expressing the coinhibitory molecule TIGIT selectively inhibit proinflammatory Th1 and Th17 cell responses. *Immunity* **40**, 569–581 (2014).
24. Weulersse, M. et al. Eomes-Dependent Loss of the Co-activating Receptor CD226 Restrains CD8(+) T Cell Anti-tumor Functions and Limits the Efficacy of Cancer Immunotherapy. *Immunity* **53**, 824–839.e810 (2020).
25. Lozano, E., Dominguez-Villar, M., Kuchroo, V. & Hafler, D. A. The TIGIT/CD226 axis regulates human T cell function. *J. Immunol.* **188**, 3869–3875 (2012).
26. Thirawatananond, P. et al. Treg-specific CD226 Deletion Reduces Diabetes Incidence in NOD Mice by Improving Regulatory T Cell Stability. *Diabetes*, https://doi.org/10.2337/db23-0307 (2023).
27. Borghi, E. et al. Construction of the World Health Organization child growth standards: selection of methods for attained growth curves. *Stat. Med* **25**, 247–265 (2006).
28. Raffin, C., Vo, L. T. & Bluestone, J. A. T(reg) cell-based therapies: challenges and perspectives. *Nat. Rev. Immunol.* **20**, 158–172 (2020).
29. Brusko, T. et al. No alterations in the frequency of FOXP3+ regulatory T-cells in type 1 diabetes. *Diabetes* **56**, 604–612 (2007).
30. Bettini, M. & Bettini, M. L. Function, failure, and the future potential of Tregs in type 1 diabetes. *Diabetes* **70**, 1211–1219 (2021).
31. Fourcade, J. et al. CD226 opposes TIGIT to disrupt Tregs in melanoma. *JCI Insight* **3**, e121157 (2018).
32. Guo, Q. et al. Engineered PD-1/TIGIT dual-activating cell-membrane nanoparticles with dexamethasone act synergistically to shape the effector T cell/Treg balance and alleviate systemic lupus erythematosus. *Biomaterials* **285**, 121517 (2022).
33. Spence, A. et al. Revealing the specificity of regulatory T cells in murine autoimmune diabetes. *Proc. Natl Acad. Sci. USA* **115**, 5265–5270 (2018).
34. Vignali, D. et al. Detection and characterization of CD8(+) autoreactive memory stem T cells in patients with type 1 diabetes. *Diabetes* **67**, 936–945 (2018).
35. Wu, B. et al. Poliovirus receptor (PVR)-like protein cosignaling network: new opportunities for cancer immunotherapy. *J. Exp. Clin. Cancer Res.* **40**, 267 (2021).
36. Shapiro, M. R. et al. CD226 Deletion Reduces Type 1 Diabetes in the NOD Mouse by Impairing Thymocyte Development and Peripheral T Cell Activation. *Front Immunol.* **11**, 2180 (2020).
37. Batlle, E. & Massagué, J. Transforming Growth Factor-β Signaling in Immunity and Cancer. *Immunity* **50**, 924–940 (2019).
38. Principe, D. R. et al. TGFβ signaling in the pancreatic tumor microenvironment promotes fibrosis and immune evasion to facilitate tumorigenesis. *Cancer Res.* **76**, 2525–2539 (2016).
39. Johnston, R. J. et al. The immunoreceptor TIGIT regulates antitumor and antiviral CD8(+) T cell effector function. *Cancer Cell* **26**, 923–937 (2014).
40. Sakano, Y. et al. Blocking CD226 regulates type 2 innate lymphoid cell effector function and alleviates airway hyperreactivity. *J. Allergy Clin. Immunol.* https://doi.org/10.1016/j.jaci.2024.01.003 (2024).
41. Mayer-Davis, E. J. et al. ISPAD Clinical Practice Consensus Guidelines 2018: Definition, epidemiology, and classification of diabetes in children and adolescents. *Pediatr. Diab.* **19**, 7–19 (2018).
42. American Diabetes Association Professional Practice Committee. 2. Classification and diagnosis of diabetes: standards of medical care in diabetes-2022. *Diab. Care* **45**, S17–S38 (2022).
43. Li, X. et al. Serum Trypsinogen Levels in Type 1 Diabetes. *Diab. Care* **40**, 577–582 (2017).
44. Shi, X. et al. Tetraspanin 7 autoantibodies predict progressive decline of beta cell function in individuals with LADA. *Diabetologia* **62**, 399–407 (2019).
45. Butler, A., Hoffman, P., Smibert, P., Papalexi, E. & Satija, R. Integrating single-cell transcriptomic data across different conditions, technologies, and species. *Nat. Biotechnol.* **36**, 411–420 (2018).
46. Stuart, T. et al. Comprehensive integration of single-cell data. *Cell* **177**, 1888–1902.e1821 (2019).
47. Korsunsky, I. et al. Fast, sensitive and accurate integration of single-cell data with Harmony. *Nat. Methods* **16**, 1289–1296 (2019).
48. Xu, C. et al. Automatic cell-type harmonization and integration across Human Cell Atlas datasets. *Cell* **186**, 5876–5891.e5820 (2023).
49. Domínguez Conde, C. et al. Cross-tissue immune cell analysis reveals tissue-specific features in humans. *Science* **376**, eabl5197 (2022).
50. Crowell, H. L. et al. muscat detects subpopulation-specific state transitions from multi-sample multi-condition single-cell transcriptomics data. *Nat. Commun.* **11**, 6077 (2020).
51. Subramanian, A. et al. Gene set enrichment analysis: a knowledge-based approach for interpreting genome-wide expression profiles. *Proc. Natl Acad. Sci. USA* **102**, 15545–15550 (2005).
52. Aibar, S. et al. SCENIC: single-cell regulatory network inference and clustering. *Nat. Methods* **14**, 1083–1086 (2017).
53. Cao, J. et al. The single-cell transcriptional landscape of mammalian organogenesis. *Nature* **566**, 496–502 (2019).
54. Trapnell, C. et al. The dynamics and regulators of cell fate decisions are revealed by pseudotemporal ordering of single cells. *Nat. Biotechnol.* **32**, 381–386 (2014).
55. Jin, S. et al. Inference and analysis of cell-cell communication using CellChat. *Nat. Commun.* **12**, 1088 (2021).

Acknowledgements

The authors thank all the participants recruited for their contributions this research. We sincerely appreciate Mr. Rui Guo from the Department of Metabolism and Endocrinology at the Second Xiangya Hospital of Central South University for his generous support and expert guidance in computer technology and analytics throughout this project. This study was supported by the National Natural Science Foundation of China (82070812 X.L., 82470871 X.L., 82170795 B.Z. and 82470814 B.Z.), the Natural Science Foundation of Hunan Province (2021JC0003 Z.Z., 2023JJ30762 X.L., and 2023JJ30805 B.Z.), and Central South University Research Programme of Advanced Interdisciplinary Studies (2023QYJC008 B.Z.).

Author contributions

X.L. (Xia Li), B.Z. and Z.Z. conceived the study. T.Z. and X.L. (Xinyu Li) performed all experiments and data analysis. K.L. and R.T. discussed and interpreted the results. T.Z., X.L. (Xinyu Li) and K.L. wrote the manuscript. X.L. (Xia Li), B.Z., Z.Z., P.L. and Q.D. critically revised the manuscript.

Competing interests

The authors declare no competing interests.

Additional information

Supplementary information The online version contains supplementary material available at https://doi.org/10.1038/s41467-024-53264-8.

Correspondence and requests for materials should be addressed to Zhiguang Zhou, Bin Zhao or Xia Li.

Peer review information *Nature Communications* thanks Roberto Mallone and the other anonymous reviewer(s) for their contribution to the peer review of this work. A peer review file is available.